Strong gravitational lensing and the stellar IMF of early-type galaxies

Dominik Leier,[1]⋆ Ignacio Ferreras,[2] Prasenjit Saha,[3] Stéphane Charlot,[4]
Gustavo Bruzual[5] and Francesco La Barbera[6]

[1]*Dipartimento di Fisica e Astronomia, Alma Mater Studiorum Università di Bologna, Viale B. Pichat 6/2, I-40127 Bologna, Italy*
[2]*Mullard Space Science Laboratory, University College London, Holmbury St Mary, Dorking, Surrey RH5 6NT, UK*
[3]*Physik-Institut, University of Zürich, Winterthurerstrasse 190, CH-8057 Zürich, Switzerland*
[4]*Sorbonne Universités, UPMC-CNRS, UMR7095, Institut d'Astrophysique de Paris, F-75014 Paris, France*
[5]*Instituto de Radioastronomía y Astrofísica, UNAM, Campus Morelia, 58190 Morelia, México*
[6]*INAF, Osservatorio Astronomico di Capodimonte, I-80131 Napoli, Italy*

ABSTRACT

Systematic variations of the initial mass function (IMF) in early-type galaxies, and their connection with possible drivers such as velocity dispersion or metallicity, have been much debated in recent years. Strong lensing over galaxy scales combined with photometric and spectroscopic data provides a powerful method to constrain the stellar mass-to-light ratio and hence the functional form of the IMF. We combine photometric and spectroscopic constraints from the latest set of population synthesis models of Charlot & Bruzual, including a varying IMF, with a non-parametric analysis of the lens masses of 18 ETGs from the SLACS survey, with velocity dispersions in the range 200–300 km s^{-1}. We find that very bottom-heavy IMFs are excluded. However, the upper limit to the bimodal IMF slope ($\mu \lesssim 2.2$, accounting for a dark matter fraction of 20–30 per cent, where $\mu = 1.3$ corresponds to a Kroupa-like IMF) is compatible at the 1σ level with constraints imposed by gravity-sensitive line strengths. A two-segment power-law parametrization of the IMF (Salpeter-like for high masses) is more constrained ($\Gamma \lesssim 1.5$, where Γ is the power index at low masses) but requires a dark matter contribution of $\gtrsim 25$ per cent to reconcile the results with a Salpeter IMF. For a standard Milky Way-like IMF to be applicable, a significant dark matter contribution is required within $1R_e$. Our results reveal a large range of allowed IMF slopes, which, when interpreted as intrinsic scatter in the IMF properties of ETGs, could explain the recent results of Smith et al., who find Milky Way-like IMF normalizations in a few massive lensing ETGs.

Key words: gravitational lensing: strong – galaxies: formation – galaxies: fundamental parameters – galaxies: stellar content – dark matter.

1 INTRODUCTION

The stellar initial mass function (IMF) is an important cornerstone of galaxy formation as it links the stellar mass and the luminosity of galaxies by defining the mass distribution of a stellar population from a single star formation burst, at birth. By controlling the ratio of low- to high-mass stars, the IMF also affects the chemical evolution of galaxies. Observationally, the IMF controls the stellar *M/L* and the conversion of typical diagnostics of star formation (e.g. nebular lines, as well as UV and FIR luminosities).

Traditionally, the IMF is considered universal, fixing its value to constraints from resolved populations in our Galaxy (e.g. Salpeter 1955; Miller & Scalo 1979; Kroupa 2001; Chabrier 2003). Constraining the IMF in distant galaxies is notably difficult because it is not possible to follow the same methodology, relying on pho-

tospectroscopic proxies, with their inherent, strong degeneracies. Although attempts at constraining the IMF go back to Spinrad (1962), only in the past decade or so it has been possible to detect a systematic trend in galaxies. There are three independent ways of constraining the IMF: (i) dynamical: based on constraints from the kinematics (see e.g. Cappellari et al. 2012); (2) lensing: focusing on strong gravitational lenses over galaxy scales (see e.g. Ferreras, Saha & Burles 2008; Auger et al. 2010; Ferreras et al. 2010; Treu et al. 2010); (3) spectroscopic: targeting selected line strengths sensitive to the presence of low-mass stars (see, e.g. Cenarro et al. 2003; van Dokkum & Conroy 2010; Ferreras et al. 2013; La Barbera et al. 2013). Over the past few years, these studies have independently found a significant change in the IMF of early-type galaxies (hereafter ETGs), with a heavier mass function in the most massive galaxies (according to the dynamical and lensing studies), more specifically with a bottom-heavy shape (according to spectroscopic studies). Scaling relations such as the Fundamental Plane can also be used to constrain the stellar IMF, although this

⋆ E-mail: dominik.leier@unibo.it

is a more indirect way that relies on assumptions about the scaling of the contribution from dark matter. Such results also suggest a heavier IMF in massive galaxies (Dutton, Mendel & Simard 2012). Theoretical models relate this trend towards a heavier IMF in the most massive ETGs with the qualitatively different fragmentation properties expected in the highly turbulent gas during the formation of the cores of this type of galaxies (see, e.g. Padoan & Nordlund 2002; Hopkins 2013; Chabrier, Hennebelle & Charlot 2014).

Although these different methods converge on the same trend, it is important to note that there are substantial degeneracies affecting them. The lensing and dynamical approaches can robustly constrain the *total M/L*, whereas the stellar *M/L* needs additional assumptions about the dark matter. Cappellari et al. (2012, 2013) find that even with the assumption of a wide range of dark matter distributions, including the case of zero dark matter, the stellar *M/L* is higher in the most massive ETGs, leading to a heavy IMF. Only for the trivial assumption of dark matter following identically the light, it is possible to discard a systematic variation of the IMF. The systematic effects in spectroscopic constraints mostly relate to the interpretation of the gravity-sensitive line strengths. These indices are measured in unresolved populations, whose spectral features are produced by blending of a large number of stellar absorption lines. Such mixtures introduce degeneracies with respect to age, metallicity, [α/Fe], or even individual abundance variations (see, e.g. La Barbera et al. 2013; Spiniello et al. 2014). Smith (2014) compared the dynamical and spectroscopic constraints to the IMF, finding residuals that correlate according to their expected systematics: the spectral index analysis correlated with [Mg/Fe], whereas the dynamical analysis correlated with velocity dispersion. However, in a follow-up paper, La Barbera, Ferreras & Vazdekis (2015) showed that this result was dependent on the population synthesis models used. In their analysis of stacked SDSS spectra, the only trend found for the IMF slope was with velocity dispersion, in agreement with the dynamical studies.

Continuing the challenge to the interpretation of the data as IMF variations, Smith & Lucey (2013) and Smith, Lucey & Conroy (2015) presented very interesting constraints on the stellar *M/L* in a reduced sample of strong gravitational lenses. These systems feature a high velocity dispersion, and therefore should lead to a bottom-heavy IMF. However, the lensing analysis produced a relatively low stellar *M/L*, leading to a standard IMF. Could these gravitational lenses be biased tracers of the populations in massive ETGs? The analysis of Posacki et al. (2015) on a sample of gravitational lenses – revisiting the work of Treu et al. (2010) – gave the trend expected from dynamical analysis of spectral line strengths, namely a heavy stellar *M/L* in massive galaxies. This controversial picture is in need of more data and analysis, to robustly assess IMF variations.

This paper addresses the mismatch from gravitational lensing by jointly comparing the lensing mass profile and the stellar mass profile. In contrast to previous studies based on the SLACS sample (see, e.g. Auger et al. 2009, 2010; Treu et al. 2010; Posacki et al. 2015) our approach is different in the derivation of both the lensing and the stellar population constraints. The former is derived from the lens geometry, applying a robust non-parametric approach. For the latter, we fit the available SDSS spectra to the latest set of population synthesis models from Bruzual & Charlot (2003) that allow for a wide range of population parameters, most importantly including two different functional forms of the IMF. We want to emphasize that unlike the studies shown above, we do not use any information on stellar dynamics to separate the stellar mass component. In addition, we present estimates from the IMF-sensitive features, following a similar procedure as in La Barbera et al. (2013), although

we note that the SNR of the spectra is not high enough for a detailed analysis on this front. The paper is structured as follows. Section 2 describes the methodology applied to determine the lensing and strellar mass profiles. Section 3 presents the sample, followed by the results of our analysis in Section 4. Finally, Section 5 includes a summary and our final thoughts on the results obtained.

2 THE MASS BUDGET FROM POPULATION SYNTHESIS AND LENS MODELLING

2.1 Photometric modelling

We downloaded pre-processed photometric *HST* data from WFPC2, NICMOS and ACS/WFC images from the MAST data base and the Hubble Legacy Archive for the sample of lenses described in Section 3. For all the lenses we used either multidrizzled data products or, if not available, the calibrated files. Strong cosmic ray (CR) features were present in most of the images. We removed them using the Laplacian Cosmic Ray Identification tool LA-COSMIC (van Dokkum 2001) with the fiducial parameter settings for every instrument. When data from multiple exposures were present, we used the IRAF *imcombine* tool (Tody 1993) with CR rejection. In many cases a more rigorous treatment for a proper CR reduction was required. For this we combined single exposures with CR rejection, which were already processed by LA-COSMIC. All lens galaxies are modelled as Sérsic profiles using GALFIT v3.1 (Peng et al. 2010), which we also use to model arcs or other light sources that might affect the surface brightness (SB) profile of the lens.

An example for a photometric model illustrating this work flow is shown in Fig. 1 for *V*-band imaging of SDSS J0946+1006. In this and several other cases, lensed images and other objects that do not contribute to the galaxy profile were simply masked out (top right panel). This was done if one of the two following criteria was fulfilled. A sufficient separation between the object and the lens galaxy, which makes other treatment unnecessary. This is evaluated by a flux profile dropping to the background level between object and lens. A mask is also employed when the residual profile – used to assess the quality of the photometric model – improves significantly below R_{min}. More information about the photometric modelling can be found in columns 3–7 of Table 3.

Unless stated otherwise, in Section 3 we use synthetic PSFs from TINYTIM (Krist 1995). We fixed the sky background in the GALFIT input to a value determined by SEXTRACTOR (Häussler et al. 2007). Low signal-to-noise objects are thus neglected, increasing the goodness of the fit for the generally bright lens galaxy. The uncertainty of the fits (see middle row of Fig. 1) is quantified by the ratio of absolute residual and original flux values within concentric annuli (middle right panel). The maximum uncertainties within R_{min} are given in column 11 of Table 3. The highest residuals in the central region of the light profiles are due to ring-like features from isophotal twist, indicating triaxial density profiles (see middle left panel of Fig. 1). The uncertainties given in the table are thus fairly overestimated. The next step involves computing the enclosed SB profile $m(<R)$ taking into account both the uncertainties from residuals and the variation of the pixel values along elliptical contours. The latter enter the calculation as we average along elliptical isophotes defined in the *H*-band model. Note we also use the *H*-band isophotes in the blue band, as we want to calculate the SB profiles consistently with respect to the same circularized radial quantity $R = \sqrt{ab}$, where a and b denote the major and the minor axis of the ellipse. For each photometric model we compute 1000 realizations of best-fitting Sérsic profile plus a randomized error, along with the cumulative
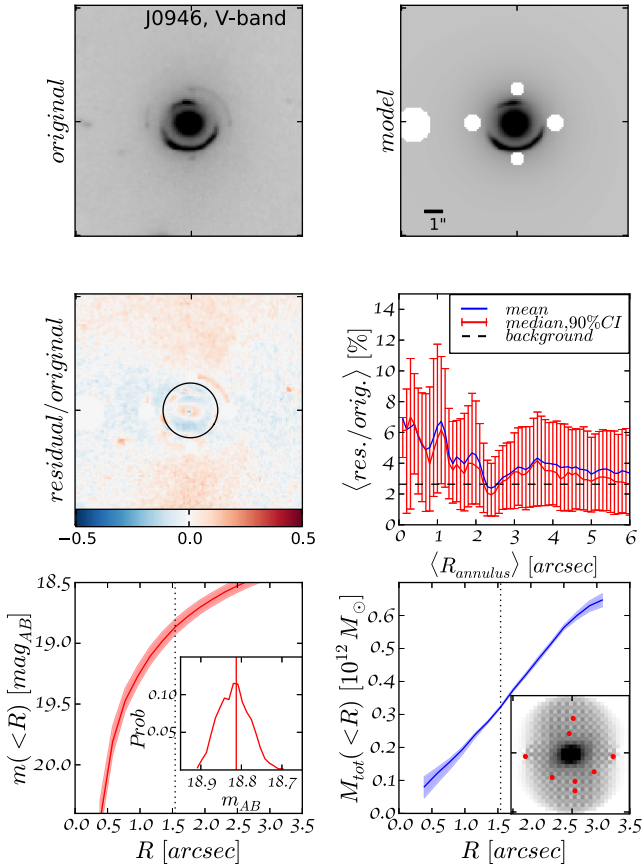
Figure 1. The production pipeline: (top left) original *V*-band photometry of the double Einstein-ring lens, J0946+1006 and (top right) its photometric model plus masked regions (white), (middle left) relative residual map, with the solid line indicating R_{min}, the radius at which the uncertainty in the mass reconstruction is minimal and (middle right) azimuthally averaged residual profile with mean (blue) and median (red) curve plus 90 per cent CI. The dashed line is an average of the RMS of the background far away from the lens. (bottom left) enclosed SB in magnitudes of the photometric model for the lens galaxy with 90 per cent CI incorporating residual uncertainty and variations along elliptical contours. The vertical dotted line indicates R_{min}. The inset graph shows normalized probabilities of the magnitudes at R_{min} from 1000 Monte Carlo realizations with vertical (red) line indicating the median of the distribution. (bottom right) Median enclosed total (lens) mass profile (blue line) with 90 per cent contours based on an ensemble of 2D mass distributions whose mean is shown in the subplot. Image positions, i.e. brightest pixels within arcs, are highlighted by red dots.

flux in AB magnitudes. We end up with an ensemble of enclosed SB profiles that allows us to obtain the median and a 90 per cent confidence interval. In summary, the photometric modelling provides a SB profile that, combined with spectral fitting (Section 2.2), yields a stellar *M/L*, that we eventually compare with the enclosed total mass profiles from lens mass reconstruction (Section 2.4).

2.2 Spectral fitting

We constrain the stellar *M/L* of the lensing galaxies by spectral fitting. The SDSS spectra of the lensing galaxies are retrieved from the DR10 DAS server.[1] The data have a typical SNR in the fitting

region between 10 and 20 per Å (see Table 1). The spectrum is corrected for foreground Milky Way reddening, adopting the standard attenuation law of Cardelli, Clayton & Mathis (1989), with the *E(B − V)* colour excess from the maps of Schlafly & Finkbeiner (2011). We derive independently the velocity dispersion of the galaxies by applying the fitting code STARLIGHT (Cid Fernandes et al. 2005), comparing the SDSS data – after bringing the wavelengths to the restframe in the air system – with the latest version of the population synthesis models of Bruzual & Charlot (2003). This version of the models incorporates updated stellar evolutionary tracks (Bressan et al. 2012; Marigo et al. 2013) and the MILES library of observed optical stellar spectra (Sánchez-Blázquez et al. 2006) to describe the properties of stars in the Hertzsprung–Russell diagram. The MILES spectral library provides a 2.5 Å resolution within the fitting window (Falcón-Barroso et al. 2011). The uncertainties in velocity dispersion are derived from 100 realizations of each spectrum, varying the flux in each wavelength bin according to their uncertainty. Our results agree with the values from the SDSS pipeline within errors (median difference with 68 per cent CI is $13.5^{+9.2}_{-37.9}$ km s^{-1}), except for J2347, for which SDSS quotes 406.6 km s^{-1}, in contrast with our 303.0 ± 64 km s^{-1}. Note that this spectrum is the noisiest one, with the lensing galaxy at the highest redshift of this sample.

In order to provide robust constraints on the stellar *M/L*, we explore a dense grid of composite populations, following a star formation history (SFH) driven by a constant star formation rate that starts at some free parameter for the cosmic age, t_{FOR} – given by its corresponding redshift, z_{FOR} – and is truncated after a time interval Δt, left as a free parameter. Metallicity and dust are also free parameters, the latter following a standard Milky Way attenuation law (Cardelli et al. 1989). Table 2 shows the parameters used and their intervals. In addition, we consider a range of choices for the IMF, following two functional forms:[2] a so-called bimodal IMF (Vazdekis et al. 1996), for which a free parameter changes both the slope of the high-mass end and the amplitude of a constant low-mass end (through the normalization), and a two-segment power-law function, for which only the slope of the low-mass end can be chosen freely. The former is a power law (with index $-\mu$) at the high-mass end, tapered off to a constant value for $M < 0.4\,\mathrm{M_\odot}$, following a spline. We refer the interested reader to appendix A in Vazdekis et al. (2003) for a detailed description of the bimodal IMF. The two-segment power law is defined as follows:

$$\frac{\mathrm{d}N}{\mathrm{d}\log M} = \mathcal{N} \times \begin{cases} M^{-\Gamma} & M \leq \mathrm{M_\odot} \\ M^{-1.3} & M > \mathrm{M_\odot} \end{cases}$$

where $\mathcal{N}$ is a normalization factor, and Γ is a free parameter that controls the fractional contribution in low-mass stars. Note that for the bimodal case, $\mu > 1.3$ represents a bottom-heavier IMF than Kroupa (2001); whereas for the two-segment power-law function, $\Gamma > 1.3$ is more bottom-heavy than Salpeter (1955). Therefore, two grids are considered, for each functional form of the IMF, each one with approximately 1.5 million models. The low-mass limit for both IMFs is set to be $0.1\,\mathrm{M_\odot}$.

Each spectrum is fit over the rest-frame region $\lambda\lambda 3700$–6000 Å, and is normalized in the interval 5200–5400 Å, taking the median of the flux values in this region.[3] The regions corresponding to

[1] http://skyserver.sdss.org/dr10/en/home.aspx

[2] Hereafter, our IMF slopes are quoted with respect to d*N*/d log *M*.

[3] We note that the available SDSS spectrum of J1100+5329 lacks flux measurements in the rest-frame window 5550–6380 Å. The spectral fit is restricted in this case to $\lambda\lambda 3700$–5400 Å. Moreover, it was not possible either to perform the analysis of the line strengths of this lens (Section 2.3).

Table 1. Properties of the lensing galaxies derived from the SDSS spectra. Column 1 is the lens ID, column 2 is the redshift, column 3 is the velocity dispersion derived from STARLIGHT runs. Column 4 is the SNR per Å measured within the normalization window (5200–5400 Å in the rest frame). The values of the parameters between columns 5 and 9 are averages with respect to all possible choices of the IMF bimodal slope (see Section 2.2). Column 10 is the best-fitting bimodal IMF slope when fitting a set of gravity-sensitive spectral indices, including additional age- and metallicity-sensitive features (see Section 2.3). All uncertainties quoted at the 1σ level.

| ID	Redshift	Vel. disp. km s^{-1}	SNR Å^{-1}	Formation redshift	Quenching redshift	[Z/H]	$E(B-V)$ mag	χ^2_ν	Bimodal IMF $\mu(1\sigma)$
J0037−0942	0.1954	277 ± 11	26.8 ± 3.4	1.6 − 5.0	1.1 − 1.7	+0.02 ± 0.08	0.05 ± 0.02	1.36	2.54 (2.12–2.96)
J0044+0113	0.1196	283 ± 17	20.1 ± 3.4	2.2 − 4.5	1.3 − 2.0	−0.10 ± 0.07	0.03 ± 0.01	1.28	2.71 (2.28–3.11)
J0946+1006	0.2219	233 ± 24	12.3 ± 1.5	0.5 − 2.1	0.5 − 0.8	−0.36 ± 0.11	0.11 ± 0.03	1.22	2.61 (1.30–3.11)
J0955+0101	0.1109	201 ± 17	11.6 ± 2.4	0.6 − 2.6	0.6 − 0.9	−0.36 ± 0.09	0.21 ± 0.02	1.57	3.05 (2.88–3.22)
J0959+0410	0.1260	170 ± 11	15.3 ± 2.7	1.3 − 5.4	1.0 − 1.6	−0.13 ± 0.41	0.16 ± 0.03	1.47	3.03 (2.84–3.21)
J1100+5329	0.3171	253 ± 55	11.7 ± 1.4	0.6 − 2.7	0.6 − 0.9	−0.19 ± 0.15	0.14 ± 0.03	1.11	–
J1143−0144	0.1060	247 ± 5	37.6 ± 5.0	2.3 − 3.3	1.1 − 1.5	+0.02 ± 0.06	0.06 ± 0.01	1.88	3.04 (2.87–3.22)
J1204+0358	0.1644	261 ± 18	14.2 ± 1.1	0.7 − 3.3	0.7 − 1.1	−0.16 ± 0.12	0.06 ± 0.02	1.06	2.21 (1.00–2.83)
J1213+6708	0.1228	257 ± 11	22.7 ± 3.1	1.5 − 5.2	1.1 − 1.8	−0.06 ± 0.09	0.06 ± 0.02	1.05	2.36 (2.00–2.82)
J1402+6321	0.2046	250 ± 13	17.8 ± 1.9	1.1 − 4.2	0.9 − 1.4	+0.08 ± 0.10	0.03 ± 0.02	1.04	2.68 (2.09–3.11)
J1525+3327	0.3583	273 ± 25	10.2 ± 2.0	0.5 − 2.1	0.5 − 0.8	−0.12 ± 0.12	0.07 ± 0.03	1.26	3.01 (2.82–3.21)
J1531−0105	0.1597	246 ± 9	22.0 ± 1.5	1.1 − 4.7	0.9 − 1.4	−0.04 ± 0.10	0.05 ± 0.02	1.92	3.01 (2.82–3.21)
J1538+5817	0.1428	178 ± 14	18.0 ± 1.7	1.7 − 4.6	1.1 − 1.8	−0.19 ± 0.45	0.13 ± 0.03	1.31	2.11 (1.40–2.79)
J1630+4520	0.2479	273 ± 16	15.7 ± 1.9	0.7 − 3.1	0.7 − 1.1	+0.04 ± 0.10	0.02 ± 0.02	1.09	2.97 (2.49–3.19)
J1719+2939	0.1807	262 ± 14	15.2 ± 1.9	0.7 − 3.2	0.7 − 1.1	−0.11 ± 0.12	0.04 ± 0.02	1.26	2.00 (0.95–2.78)
J2303+1422	0.1553	276 ± 37	14.9 ± 1.4	0.7 − 3.2	0.7 − 1.1	−0.01 ± 0.11	0.09 ± 0.03	2.38	2.82 (2.19–3.15)
J2343−0030	0.1807	245 ± 11	17.8 ± 2.1	1.2 − 4.6	1.0 − 1.5	+0.09 ± 0.09	0.06 ± 0.02	1.35	2.41 (1.59–3.01)
J2347−0005	0.4167	303 ± 64	8.8 ± 2.2	0.6 − 2.9	0.7 − 1.0	−0.14 ± 0.42	0.12 ± 0.04	1.67	0.30 (0.30–2.10)

Table 2. Model parameters used for the grid of SFHs. Each model is defined by a constant star formation rate, $\psi(t) = \psi_0$ starting at cosmic time t_{FOR}, given by a formation redshift z_{FOR}, and stopping at $t = t_{FOR} + \Delta t$.

| Observable	Parameter	Range	Steps
Formation redshift	z_{FOR}	[1,10]	32
Time-scale	$\Delta t/$Gyr	[0,3]	32
Metallicity	$\log Z/Z_\odot$	[−0.5, +0.3]	12
Dust	$E(B-V)$	[0.0,0.3]	12
IMF Slope (Bimod.)	μ	[0.8,3.3]	9
IMF Slope (2-PL)	Γ	[1.0,2.6]	10
	Number of models (Bimodal)		1327 104
	Number of models (2-power laws)		1474 560

emission lines at the redshift of the background source are masked out. See Fig. 2 for an illustration of a typical case of spectral fitting. The process starts with a small grid of (dustless) simple stellar populations, exploring a range of ages (t ∈ [0.5,10.5] Gyr; 30 steps) and metallicities ([Z/H] ∈ [−0.5,+0.3]; 6 steps), after which the best fit is used to discard data that depart more than 4σ from the fit. Typically very few pixels are masked out from the process. The dense grid of models (Table 2) is then run, creating a probability distribution function from the comparison with each model. The constraint on *M/L* follows a Bayesian approach, exploring a grid of composite models as described above. For each model taken from the grid, a synthetic spectrum is created at the same velocity dispersion as the observed galaxy, and fitted via a standard likelihood function.

$$\mathcal{L}(\pi_i) \propto e^{-\chi^2(\pi_i)/2}, \tag{1}$$

where χ^2 is the standard statistic comparing the observed spectrum, $\Phi(\lambda)$, with a 1σ uncertainty per wavelength bin,
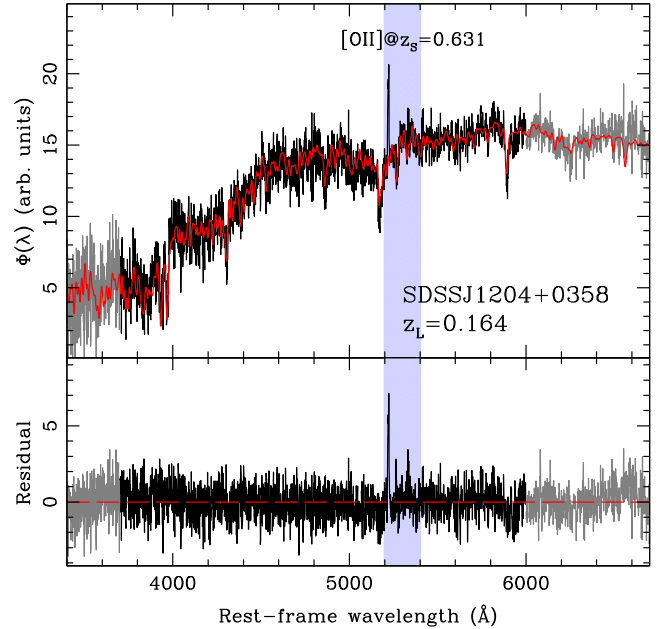
Figure 2. Example of a spectral fit applied to constrain the stellar *M/L*. Top: the SDSS spectrum of J1204+0358 (z = 0.164) is shown as in black/grey (the black region denotes the spectral window where the fitting is done). The best-fitting result for a Kroupa-like IMF (bimodal IMF function with $\mu = 1.3$) is shown in red. The normalization region appears in blue. Bottom: residual, measured as $(\Phi - \Phi_{FIT})/\Delta\Phi$. Note that the only significant residual appears in the line at $\lambda_{REST} \sim 5220$ Å, which corresponds to [O II] emission from the background source at $z = 0.631$. These regions are masked out from the fitting procedure (see text for details).
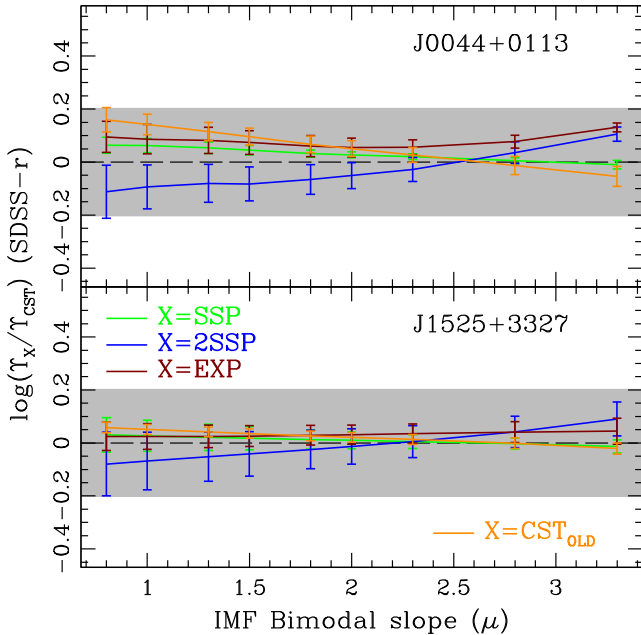
Figure 3. Effect of the star formation history on the constraint of the stellar *M/L* via spectral fitting. The stellar *M/L* measured in the SDSS *r* band is shown for lenses J0044+0113 (top) and J1525+3327 (bottom) as a function of the IMF bimodal slope, μ. We show the difference between the *M/L* of a given model (labelled *X*), and the fiducial one (CST, see text for details). Note the model with two populations (2SSP, allowing for a young stellar component) gives in general lower values of *M/L*. The orange line represents a comparison with models where the CST parametrization is forced to produce old stellar ages (see text for details). The grey shaded area corresponds to a ± 0.2, dex interval, and encompasses the overall difference in $\log \Upsilon$, i.e. around a factor $2.5\times$ in *M/L*.

$\sigma[\Phi(\lambda)]$; and the model spectrum for a choice of parameters $\Phi_{\mathrm{MOD}}(\lambda, \pi_i)$:

$$\chi^2 = \sum_\lambda \frac{[\Phi(\lambda) - \Phi_{\mathrm{MOD}}(\lambda; \pi_i)]^2}{\sigma^2[\Phi(\lambda)]} \qquad (2)$$

$\{\pi_i\}$ represents any of the parameters that define the model, such as IMF slope, age, metallicity, etc. From the likelihood we derive the values of the parameters, given as probability-weighted quantities, namely:

$$\langle \pi_j \rangle = \frac{\int \mathcal{L}(\pi_i)\pi_j \prod_i \mathrm{d}\pi_i}{\int \mathcal{L}(\pi_i) \prod_i \mathrm{d}\pi_i} \qquad (3)$$

where $\prod_i \mathrm{d}\pi_i$ represents the integration element extended to all the parameters that define the models.

Note that we are modelling massive ETGs, notoriously homogeneous systems with old, metal-rich, and passively evolving populations (see, e.g. de la Rosa et al. 2011). Therefore, our constraints on the *M/L* are not sensitive to the functional form adopted for the SFHs. To quantify in more detail this point, we ran three additional sets of grids involving simple stellar populations (SSP; 65,536 models), exponentially decaying SFHs (EXP; 262,144 models), and a composite of two stellar populations, involving a young and and old one, with the mass ratio of the two kept as an additional free parameter (2SSP; 524 288 models). All use the same steps and range for metallicity and dust as the fiducial model. Fig. 3 shows the difference between these choices of SFH on the predicted *M/L*, given here in the SDSS-*r* rest-frame, for two lenses: J0044+0113 and J1525+3327, adopting the bimodal functional form of the IMF.

Note the 2SSP models mostly yield the lowest values of *M/L*, as in this case a significant contribution from very young stars is allowed. The EXP models applied to old populations tend to slightly overconstrain the tail of the exponential, producing very short star formation time-scales (an issue discussed in detail in Ferreras et al. 2012), leading to higher *M/L*. Our fiducial models (labelled CST, after constant + truncated SFH), and the simpler SSP grid give intermediate results. We also include, for reference, a comparison (orange lines) between the fiducial models and those with the same parametrization (i.e. CST), where the formation redshift only probes the $z_{\mathrm{FOR}} \in [5,10]$ interval and the star formation duration is restricted to $\Delta t < 1.5$ Gyr. These models – labelled $\mathrm{CST_{OLD}}$ in the figure – represent a case where one imposes a prior enforcing old stellar ages in these systems. The grey shaded area extends over a ± 0.2 dex variation, and roughly gives the range of variation of the stellar $\log \Upsilon$, implying differences up to a factor $2.5 \times$ in *M/L* regarding the different model parametrizations. Notice the non-trivial behaviour of the differences between the SFH parametrization and the IMF slope. Spectral fitting of a bottom-heavy IMF tends to produce younger ages (Ferré-Mateu, Vazdekis & de la Rosa 2013), therefore complicating the variation of *M/L*.

Regarding systematic differences with respect to independent population synthesis models, we refer the reader to fig. 5 in Ferreras et al. (2010), where the *H*-band stellar *M/L* was compared among several, independent models, finding good agreement, with variations at the level of 10 per cent, without any systematic trend.

Table 1 lists the constraints on the stellar population parameters for all lenses. Note the results are obtained from the fiducial CST models. The age, duration of star formation, metallicity and intrinsic colour excess are shown as probability-weighted quantities, including their RMS as an error bar. The reduced χ^2 of the fits is also shown. The fitting procedure involves between 600 and 2200 data points. Fig. 4 shows a comparison of the mass estimates (both lensing and stellar) with Auger et al. (2009). Our stellar (lensing) masses enclosed in R_{Ein} are 0.38 dex (0.05 dex) lower than those of Auger et al. (2009) on average, with a scatter of 0.14 dex (0.13 dex).

Note that Auger et al. (2009) use broad-band colours to constrain stellar masses, with a set of exponentially decaying SFHs (i.e. the EXP models presented above). It is a well-known fact that such models usually overestimate stellar masses in the typical quiescent populations expected in ETGs, since the tail of the exponential – that would result in younger populations – tend to be suppressed by the passive-like colours (or spectra) found in these galaxies. As there is only one parameter to control this, the model produces very short values of the time-scale, τ, resulting in older populations and hence higher values of the stellar *M/L* (see Fig. 3). In Ferreras et al. (2012) this issue is explored in detail for the case of a massive galaxy at $z \sim 2$, where it is found that other parameterizations of the SFH, such as truncated models, analogous to the CST case explored in this paper, produce more realistic SFHs. Pacifici et al. (2015) also find that EXP-type models overproduce stellar masses. In addition, simulations of galaxy formation tend to disfavour exponentially decaying SFHs (Simha et al. 2014). However, Fig. 3 only shows the variations in *M/L* regarding the parametrization of the SFH. Therefore, it cannot account in full for the offset between our stellar masses and those from Auger et al. (2009) – shown in Fig. 4. Differences in the methodology – photometric modelling restricted to a few bands versus full spectral fitting, the different model fitting method: sparse sampling of likelihood space via MCMC versus a full search over a large volume of parameter space, and the application of priors on the stellar population parameters (in Auger et al.
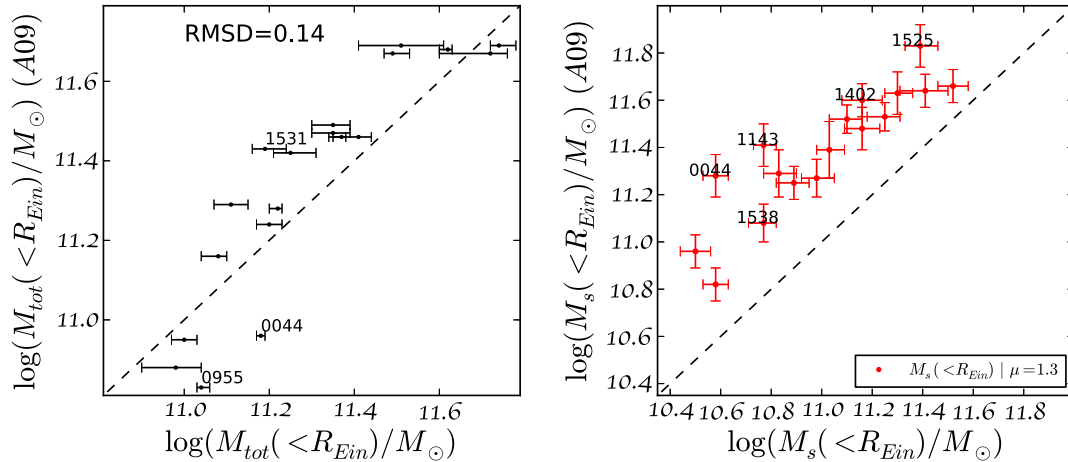
Figure 4. Left: comparison of lens masses enclosed in R_{Ein} according to Auger et al. (2009) and this study. The *x*-axis error bars show the 90 per cent confidence interval for an ensemble consisting of 300 models. Right: comparison of the stellar mass estimates enclosed in R_{Ein} from Auger et al. (2009) (based on a Chabrier 2003 IMF, transformed to Kroupa by adding +0.05 dex) and this study. The red dots indicate stellar masses based on a Kroupa (2001) IMF ($\mu = 1.3$). The *x*-axis error bars indicate again the 90 per cent confidence interval. Note that J2343 is not included in the lens sample of Auger et al. (2009). We only label those lenses with the largest offsets.

2009, but not in this paper) – will introduce systematic differences in the retrieved stellar masses.

2.3 Constraints on gravity-sensitive features

The SNR of the data ($\sim$10–30 per Å) are acceptable for a constraint on the stellar *M/L* through spectral fitting (previous sub-section), but it is not large enough to perform a detailed analysis of gravity-sensitive features, where values of the SNR an order of magnitude higher are typically needed. Although the focus of this paper is the comparison of the stellar *M/L* from spectral fitting and the total *M/L* from the lensing analysis, we include here the analysis of the gravity-sensitive spectral indices, to test for possible systematic differences. We stress that this is only meant as an illustration of the properties of our lensing galaxies on this issue. We apply the same methodology as in La Barbera et al. (2013), with the publicly available MILES-extended models of Vazdekis et al. (2012) for a bimodal IMF parametrization.

We start with a fit of the spectra with an SSP model, fitting simultaneously adjacent spectral windows $\sim$1000 Å wide each, at the velocity dispersion of each lens (Table 1). The best-fitting models are used to replace those spectral regions where some emission from the source is expected or where prominent sky residuals are found in the observed spectrum. A variety of line strengths is then fitted with SSP models to constrain the IMF. We fit simultaneously: Hβ_o, HgF, [MgFe]′, TiO1, TiO2$_r$, Mg4780, Fe4531 and NaD, including [Ti/Fe] as a free fitting parameter. Notice that the low SNR of the spectra does not allow us either to obtain an accurate estimate of [α/Fe], or to include NIR gravity-sensitive features in the analysis, such as the Na doublet ($\lambda \sim 8200$ Å), and the Ca triplet ($\lambda \sim 8600$ Å). For this reason, we do not include [Na/Fe] as an extra fitting parameter to the line-strengths, adopting, instead, a mild 'residual' [Na/Fe] = 0.07 dex, and a fixed value of [α/Fe] = +0.2 for all lenses, typical of ETGs at $\sigma \sim 250$ km s^{-1}. We note that this overabundance in [Na/Fe] is considered *in addition* to the contribution from the supersolar [α/Fe] expected in massive ETGs.

The effect of a non-solar [α/Fe] follows the empirically based corrections to the indices presented in La Barbera et al. (2013), whereas the effect of individual abundances ([Ti/Fe] and [Na/Fe])

is determined from the models of Conroy & van Dokkum (2012a). We emphasize that this methodology follows closely the analysis of La Barbera et al. (2013); whereas other groups find significantly different values of [Na/Fe] (see, e.g. Conroy, Graves & van Dokkum 2014). Nevertheless, this part of the analysis does not alter our conclusions within the error bars of the line strength measurements. The results for a bimodal IMF are shown in the last column of Table 1, where the interval in brackets delimits the 1σ confidence interval. As expected, the error bars are rather large. Nevertheless, we detect a similar trend as in previous studies based on gravity-sensitive indices, with a significant trend towards a bottom-heavy IMF.

2.4 Lens modelling

The lenses were modelled by the free-form method PIXELENS (Saha & Williams 2004; Coles 2008). The main input data to PIXELENS consists of the positions of point-like features that are multiply imaged. PIXELENS then finds possible mass distributions that exactly reproduce the multiple-image data. Each mass distribution is built out of $\sim$500 mass tiles, and is required to be concentrated about the brightest point of the lensing galaxy, but is otherwise free form. No other information about the light from the lensing galaxy is used.

For each lens, the lens-modelling output consists of an ensemble of $\sim$200 mass maps. The model ensembles contain a diverse set of possible models that would be consistent with the data, and hence explore the model uncertainty[4] The enclosed-mass profiles are typically tightly constrained near the Einstein radius, and widen out at smaller and larger radii in a characteristic butterfly shape. The enclosed mass within the Einstein radius provides an upper limit on the stellar mass. This is the basis of the IMF constraints in this paper.

Parametric lens models have been used by other workers (Auger et al. 2010; Treu et al. 2010; Posacki et al. 2015; Smith et al. 2015) as the basis of IMF constraints. As an example, Fig. 5 compares the

---

[4] The GLASS code (Coles, Read & Saha 2014) uses the same basic strategy as PIXELENS but improves the ensemble-sampling strategy. The difference is unimportant for this work.
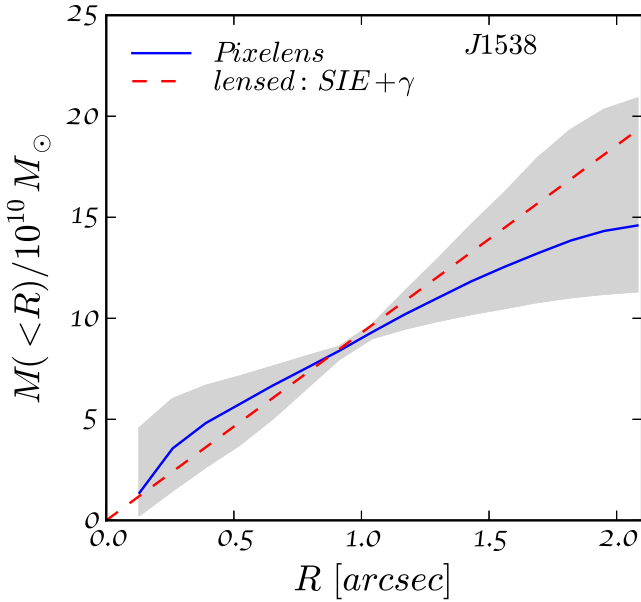
Figure 5. Comparison of the enclosed mass profiles reconstructed by PIXELENS and LENSED for the lens J1538+5817. The blue solid line indicates the PIXELENS ensemble median with 90 per cent confidence interval (shaded area). The red dashed line shows a Singular Isothermal Ellipsoid (SIE) model plus shear.

free-form enclosed-mass profiles from PIXELENS with a parametric model using the reconstruction code LENSED (Tessore, Bellagamba & Metcalf 2015), for J1538+5817. (Further comparisons of this kind can be found in Leier, Ferreras & Saha 2012). As expected, the parametric model falls within the range delineated by the free-form models.

Possible criticisms of our approach are (a) the lens models do not use data on extended images, only on point-like features, and (b) no kinematic information is used. It turns out, however, that PIXELENS models actually produce reasonable reproductions of extended images (e.g. fig. 3 of Ferreras et al. 2008) and velocity dispersions (e.g. fig. 5 of Leier 2009). So these criticisms appear not to be severe.

An advantage of our approach is that it avoids assuming any particular parametric forms for the dark-matter distribution. In the appendix, Fig. A1 presents the models fed to PIXELENS for the lensing analysis. We note that 6 of the 18 lenses include external shear in the lensing analysis, with further information given in Table A1.

3 THE SAMPLE

Our working sample comprises 18 strong gravitational lenses from the Sloan Lens ACS data set (SLACS, Bolton et al. 2006), choosing targets that are suitable both for photometric modelling and lens reconstruction. Our methodology demands the following selection criteria.

(a) Availability of pre-processed photometric data in multiple bands, preferably *H*, *V* and *I*, which permits the production of photometric models with sufficient quality estimated by the residual-to-original flux ratio of $\lesssim 15$ per cent (details are given in Sections 2.1 and 3).

(b) A sufficient separation between the lens and lensed images in order to extract uncontaminated photometric estimates from the

lens, as degeneracies between the two components might occur during the SB fits.

(c) An unequivocal determination of the position of the lensed images – specifically their brightest pixels – which are input to the lens mass reconstruction.

The strongest criterion is in fact (b), leading to a reduction of ∼46 per cent of the sample size of SLACS lenses from Auger et al. (2009). We would like to emphasize that this selection constraint does not lead to a biased distribution of $R_{\rm eff}/R_{\rm Ein}$ or to bias towards larger dark matter fractions. To illustrate this point, we compare the median (± 90 per cent CI) of $R_{\rm eff, I}/R_{\rm Ein}$ for the whole SLACS sample, $1.44^{+1.18}_{-0.62}$, with the sample used in this study, adopting independently determined $R_{\rm eff}$ and $R_{\rm min}$, with a median (± 90 per cent CI) of $1.44^{+2.18}_{-0.37}$. A Kolmogorov–Smirnov test comparing the Auger et al. (2009) sample and our sample yields a two-tail *p*-value of 78 per cent in favour of the two samples being drawn from the same distribution. Therefore, we do not expect any additional biases with respect to the parent SLACS sample.

We discuss in more detail the lenses and their environment below. Readers more interested in the results of our study should proceed to Section 4.

3.1 The lenses

We briefly discuss below the properties of the lenses studied in this paper. Note that for the lens modelling performed in this paper, we are mostly concerned about obtaining good fits to the SB profile within a region where the lensing uncertainties are smallest. Hereafter, we refer to this area as the region of interest, which roughly represents the Einstein radius.

SDSS J0037-0942 is a galaxy with a doubly lensed image configuration. With a redshift of ∼0.195 it is situated in the foreground of the cluster ACO 85 at $z = 0.55$ with 10 Galaxies along the line of sight within a 1 Mpc projected distance (Slezak et al. 1998). Auger (2008) finds five galaxies along the line of sight, within a 30 arcsec distance to the lens. The brightest of these, a late-type galaxy, can be seen in a WFPC2 *I*-band image. However, the SIMBAD data base does not list this galaxy as a member of the cluster. In fact, the nearest object listed in the data base is 1 arcmin to the South of the lens. Since the shear component does not point into the direction of the late-type galaxy either, we can assume that it does not influence the lens mass reconstruction. The central region of the lens galaxy is modelled with good accuracy, as the fractional residual map (defined as the residual with respect to the best fit, divided by the original map) yields, average deviations around 5 per cent along circular contours in *H*-band and being slightly higher in the *I*-band residual map (∼10 per cent). For the ACS/WFC *I*-band image we used drizzled data from the MAST data base that still contain CRs. As the single exposure could not be retrieved, we decided to remove the CRs via LA-Cosmic (van Dokkum 2001). Since no non-saturated nearby stars without CR pollution were close, we decided to use a PSF created by TINYTIM. The profile is comparable in quality to the *H*-band fits.

SDSS J0044+0113 features one distinct arc and one image close to the centre. The arc has been modelled using the new features of GALFIT, resulting in residuals below 4 per cent in both bands within the region of interest. The small uncertainty stays below the RMS of the background, measured in the outer regions of the images. The image close to the centre of the lens can be seen in the residual of the *V*-band photometry as a 10 per cent spike, but it does not show up in the *H*-band, as it is either too faint to be

seen in infrared or the SB fit incorporates it. However, masking out this region does not change the fit significantly. This lens is located in a cluster environment (Rines et al. 2003) The closest neighbour associate to the same cluster lies ∼1.5 arcmin to the South. Based on the photometry, there seem to be a few faint and small elliptical galaxies within 30 arcsec. However, they do not contribute to the model fit. The PSF was simulated via TINYTIM.

SDSS J0946+1006, also called the 'Jackpot', is a double Einstein Ring lens located in a complex environment. It is not known to be member of a cluster. The lens galaxy seems to be the brightest galaxy in its neighbourhood (Gavazzi et al. 2008), and it is accompanied by at least one bright galaxy whose photometric redshift is consistent with the redshift of the lens galaxy. This companion is located ∼40 arcsec South-West of the lens and its perturbed isophotes suggest a recent fly-by and tidal interaction with it. Other nearby light sources are not know to be at the same redshift. In the photometric models, the brightest areas of the outer arcs are masked out. The inner arcs are modelled with GALFIT. We also mask out three additional objects in the vicinity, which are less than 8 arcsec away from the centre of the lens. The residual map in the *H*-band shows a diffuse cloud around a nearby object, South-East of the lens, which could be debris from the aforementioned fly-by. As a result, the residual maps show uncertainties along circular contours around 5 per cent in the region of interest. The PSF was created by TINYTIM. The brightest pixels of the outer and inner arcs have been used to model the lens. The IMF of the 'Jackpot' has been studied also by Sonnenfeld et al. (2012) and was found to be in agreement with a Salpeter function.

SDSS J0955+0101 is a structured late-type spiral with a disc and bulge seen almost edge-on. One extended arc with three brighter knobs is located ∼1.3 arcsec South-West of the light-centroid of the lens. This arc is masked out in the modelling of the *I*-band image, but fitted with GALFIT in the *H*-band frame. In both bands the lens galaxy is modelled as a composite of Sérsic along witg an edge-on disc. The residual map shows that the Sérsic-plus-disc model describes the galaxy well in the region within 1 arcsec, as the median residual profile stays below 10 per cent in both bands. There is a compact group of galaxies North-West of the lens with four members (McConnachie et al. 2009). We can determine the photometric redshift of the two brightest member galaxies by means of the BPZ code (Benítez 2000), getting $z_A = 0.11^{+0.06}_{-0.06}$ and $z_B = 0.08^{+0.03}_{-0.04}$ within a 68 per cent confidence interval, therefore both are consistent with the redshift of the lens galaxy. The external shear points along the North-West direction is consistent. The lens model uses the brightest pixels of the three knobs in the arc and one image close to the centre. A TINYTIM PSF has been used in both bands.

SDSSJ0959+0410 is a lens with a doubly lensed background galaxy. In the visual band its surrounding is highly structured with several clumps and plumes, apparent in the residual maps. As we are not able to model them one by one photometrically, we mask them out. In the *H*-band this was not necessary, although there are ringlike features suggesting a recent tidal interaction or merger. However, there does not seem to be any nearby galaxy at the same redshift. The closest galaxies might be in a compact group, at a 5.5 arcmin projected distance towards the North-West. Auger (2008) report five objects along the line of sight, within 30 arcsec. None of these affect the photometric modelling. Consequently, the median residual profile stays well below 10 per cent in the region of interest in all bands. For the mass model we use the centroid of the distinct images. A TINYTIM PSF was used.

SDSS J1100+5329 is a cusp quad configuration lens with a large 180° arc in which several distinct features can be found. The arc

is about 1.8 arcsec from the centre of the lens, which corresponds to ∼8 kpc at its redshift. This is certainly an extreme value, being one of the largest Einstein radii in SLACS (Auger et al. 2009). We masked out several nearby, small objects. The residuals stay below 5 per cent (*H*-band) and below 10 per cent (*I*-band) in the central region of the lens. The lens is in a close encounter with another galaxy just 3.9 arcsec towards the North-East. A tidal arm extends from the companion in a way that might contribute light to the arc. A nearby star also in the North-East direction is too faint to substantially alter the fits. A visual inspection of a 30 arcsec region around the lens shows about 20 objects, most of them South-East of the lens. They seem to be part of a compact group of galaxies. Considering the complexity of the environment, it does not come as a surprise that the residuals of the fits show a quickly increasing trend beyond the Einstein radius. However, we find a good *H*-band model, with an average residual at ∼5 per cent of the original SB in the central region, and an *I*-band model with a residual below 10 per cent. A TINYTIM PSF was used.

SDSS J1143-0144 exhibits two large arcs with radii 2.4 and 1.7 arcsec, respectively. The latter is very faint compared to its environment, complicating the SB modelling. The larger and more pronounced (45°) tangential arc has a small radial arc as a counterpart. Both the radial arc and the brighter spots in the faint arc have been masked out for the photometric model. We use this doubly imaged configuration as an input for the lens reconstruction. The lens galaxy is known to be the brightest cluster galaxy of ACO 1364, with at least 12 companions within 1 arcmin. The high density environment and extended low SB envelope often found around cD galaxies (Seigar, Graham & Jerjen 2007) explains why with increasing radius, a single Sérsic profile does not provide a good fit anymore. Note that we find a ring feature with a radius of approximately 0.8 arcsec in all three bands which deviates ∼10 per cent at most from the model fit.

SDSS J1204+0358 produces a system of two arcs, whose brightest pixels are used as input to the free-form lens model. There are many objects along the line of sight, probably part of the nearby (45 arcsec) distant compact galaxy group, which in turn may be associated with the galaxy cluster ACO 1463, whose centre lies only 109 arcsec South of the lens. There is one late-type galaxy (5 arcsec) appearing almost edge-on. Judging by its warped disced, it might be in tidal interaction with the lens. There is a fair amount of small sources in the vicinity of the lens, but the photometric models are hardly influenced by them. The arcs could be modelled and subtracted by GALFIT, giving one of the best model fits with average residuals in the *V*-band, around 3 per cent over a radial range of 4 arcsec. In the *H*-band an extended envelope is evident, with a different isophotal orientation. However, within the Einstein radius the Sérsic profile leaves relative residuals below 5 per cent.

SDSS J1213+6708 is another doubly imaged background galaxy, which forms one arc and another image close to the centre. The *V*-band modelling is complicated by an isophotal twist, leading to larger residuals at the centre. As this does not occur in the *H*-band image for a Sérsic profile with comparable parameters, we tend to discard other model fits that give a better agreement in the centre, but worse results in the outskirts of the lens. The stellar mass estimates from the *H*- and *V*-band are thus very similar. As the arcs are faint but clearly visible in the residual map of the *H*-band model, we mask them out. The residuals stay below 10 per cent (15 per cent) in the *H*-band (*V*-band) within the region of interest. Not much is known about the environment of the lens, however there seem to be a at least two galaxies along the line of sight, about 0.5 arcmin East

of the lens. There is also a saturated star nearby whose wings are marginally visible in the *V*-band residual.

SDSS J1402+6321 exhibits two extended arcs which form almost an Einstein ring around the lens galaxy. In *H*-band they are invisible. In *I*-band we mask them out. Sérsic fits yield good results, below 5 per cent in both bands. Auger (2008) finds six objects within 30 arcsec along the line of sight. There are no known redshifts for these objects. The positions of four distinct knobs in the arcs are taken as input to the lens modelling.

SDSS J1525+3327. The *H*-band photometry is modelled with residuals below 10 per cent and the *V*-band residuals stay below 5 per cent, except for one spike around the radius of the arc, which was largely masked out. There are at least five objects within a projected 35 arcsec distance to the lens, and additional light extending towards two of them. The closest object in projection, quite possibly interacting with the lens galaxy, is just 2.8 arcsec North-West of the lens. We mask it out and model the arc and one counter image close to the centre as it was done in Newton et al. (2011). Furthermore, this lens appears, in projection, close to a cluster, with its BCG about 45 arcsec South-West of the lens. Its redshift ($z \sim 0.22$) is however much lower (Gal et al. 2003).

SDSS J1531-0105 is almost an Einstein ring with three extended features, two bright ones and one faint but more extended arc indicating a fold caustic configuration. Judging by the present photometry there are at least three stars and more than six galaxies within a radius of 30 arcsec along with additional faint sources, one of which could even be another arc in the lens configuration. All these were masked to get a good photometric model. However, we model the lens as a three image configuration as there are no distinct maxima in the light distribution of the faint arc. The median residual profile in *V*-band is at the 5 per cent level, whereas the *H*-band residual profile shows a prominent bump, increasing to 10 per cent as a result of the more extended shape of the arc in this band. It should be noted that there is a compact galaxy group ~ 2 arcmin South of the lens, confirmed at the same redshift as the lens galaxy (McConnachie et al. 2009). The physical distance between the lens galaxy and the group is ~ 320 kpc, i.e. close enough to be affected by its gravitational pull.

SDSS J1538+5817 shows an Einstein ring with four distinctly bright areas and a doubly imaged source at different redshifts. Recent tidal interaction, possibly a merger, seems to have left an extended arm of debris with several lumps of higher density. The closer environment (<30 arcsec) of the lens is populated with about 10 objects on the line of sight. The next brightest galaxy in the field is only 15 arcsec South-East. The isophotes of the lens do not seem to be affected by it. The lens galaxy is surrounded by a patchy envelope of light which cannot be easily modelled by an additional profile. As a consequence the residual stays around 5 per cent within the Einstein ring, beyond which it increases drastically up to 20 per cent. Grillo et al. (2010) estimated the enclosed mass profile using the ring and an additional image system based on a background object at different redshift. Their SIE fit gave $\log (M_{\mathrm{Ein}}/\mathrm{M_\odot}) = 10.91^{+0.01}_{-0.02}$ and their PixeLens model yields an enclosed mass within the Einstein radius of $\log (M_{\mathrm{Ein}}/\mathrm{M_\odot}) = 10.93^{+0.01}_{0.01}$. This is only slightly lower than ours (using the quad configuration) with $\log (M_{\mathrm{Ein}}/\mathrm{M_\odot}) = 10.96^{+0.01}_{0.01}$. The latter is however in agreement with the results in Auger et al. (2009). We model the lens assuming a $SIE + \gamma$ profile and obtain a value of 10.97. Grillo et al. (2010) determine a total stellar mass of $10^{11.3}$ M$_\odot$, Auger et al. (2009) come up with $10^{11.03 \pm 0.08}$ M$_\odot$ for a Chabrier IMF and $10^{11.28 \pm 0.08}$ M$_\odot$ for a Salpeter IMF.

SDSSJ1630+4520 is a lens with two extended arcs, an outer one that almost completes an Einstein ring and an inner one. Both have two brighter regions which we use to model the lens. Auger (2008) finds four objects within 30 arcsec along the line of sight. In the *H*-band the data are noisy. The *I*-band, however, allows for a very good fit, with a flat residual profile below 4 per cent within the Einstein radius. Despite the high amount of noise, the *H*-band model yields stellar masses in good agreement with the *I*-band results.

SDSS J1719+2939 exhibits a quadruply lensed image configuration. The brightest pixels serve as input to PixeLens. There are very few faint objects within a 30 arcsec radius from the lens. The closest one (~ 3.8 arcsec to the South-East) has distorted isophotes in the *V*-band, suggesting a tidal interaction. It is consequently masked out. The next bright objects are a barred spiral galaxy ~ 33 arcsec to the South-East, and an ETG, ~ 38 arcsec towards the North-West. There is also a nearby saturated star whose PSF wings extend to the fitting area around the lens. It has however no strong impact on the model fit. We obtain good Sérsic-fits with relative residuals <5 per cent ($\lesssim 7$ per cent) in the *V*- (*H*-)band within the ~ 1.3 arcsec Einstein radius.

SDSS J2303+1422 shows two arcs with two distinct bright peaks each. Auger (2008) finds six objects within 30 arcsec of the lens. There is a faint elongated object 4.4 arcsec North of the lens which could be in tidal interaction with the lens. The arcs have been modelled in the *V*-band but masked out in the *H*-band. We obtain perfect fits with residuals <5 per cent, which is below the RMS of the background.

SDSS J2343-0030 is a quadruply imaged source in cusp caustic configuration which forms a partial Einstein ring. The lens galaxy belongs to a galaxy cluster (Geach, Murphy & Bower 2011) and has one nearby companion only 7 arcsec towards the South-West, a late-type galaxy seen almost edge-on. Within a radius of 30 arcsec, we can identify another galaxy that seems to be late-type, whose colour suggests that it is also part of the cluster. This lens has only been modelled in the *V*-band. No NICMOS data were available from the archive. We are able to create a photometric model of the arc, which results in the usual flat median residual uncertainty of $\lesssim 6$ per cent over a radial range of about $2R_{\mathrm{Ein}}$.

SDSS J2347-0005 is a doubly imaged lens configuration. A galaxy cluster at a lower redshift ($z = 0.2637$) is located about 100 arcsec South-West of the lens. Another galaxy with a similar redshift to the lens appears 75 arcsec towards the West (Drinkwater et al. 2010). *V*-band data reveal a multitude of sources on the line of sight, with different sizes and morphologies. About 15 arcsec South of the lens galaxy we find two late-type galaxies that are about to merge. At a distance of 16.3 arcsec to the North, we find another late-type galaxy. The *H*-band photometry gives a good fit, yielding residuals $\lesssim 7$ per cent in the region of interest. The *V*-band, however, reveals a complex substructure environment, which could not be modelled photometrically. Consequently we largely masked most of the arcs and SB peaks out. The data appear very noisy in this band, explaining the sharp increase in the residual values beyond 1.5 arcsec. As a consequence, the stellar mass estimate based on the *H*-band is ~ 13 per cent larger than the one based on the *V*-band.

4 DISCUSSION

Fig. 6 shows the stellar mass for the whole sample as a function of the IMF slope, adopting either a bimodal shape (left) or a two-segment power-law function (right). These estimates correspond to projected masses within an aperture, R_{min}, where the uncertainty
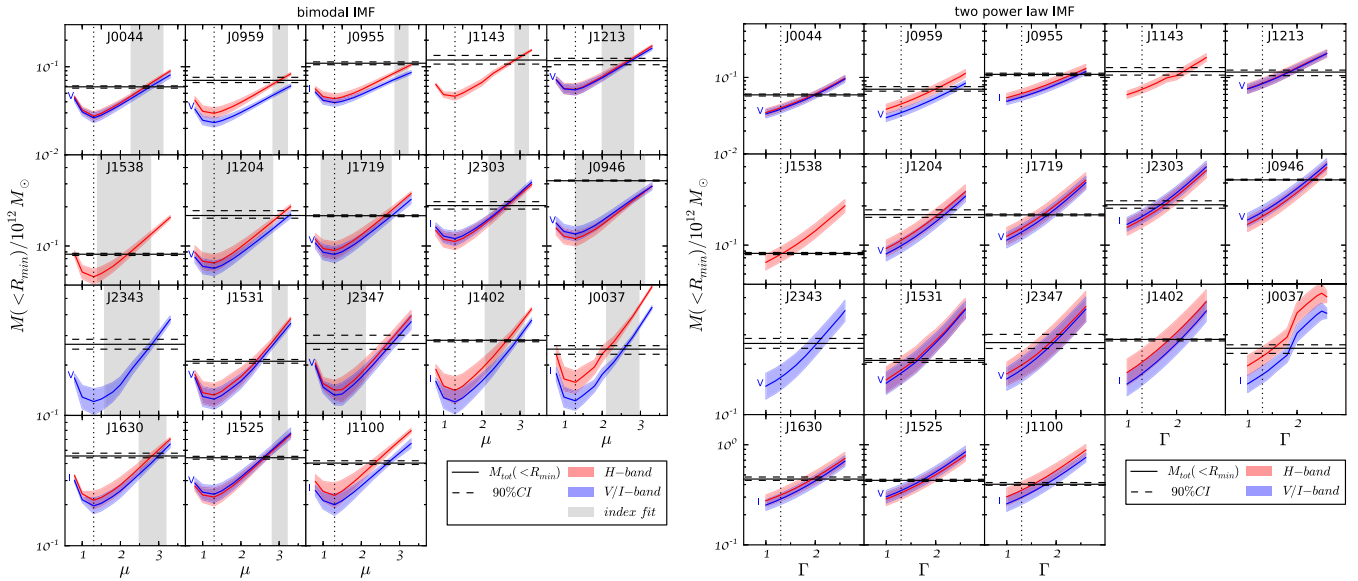
Figure 6. Left: stellar mass from *H*-band (red) and *V/I*-band (blue) population synthesis compared to the total enclosed mass from lensing for which the median and a 90 per cent CI (solid and dashed horizontal lines) is given. Vertical dotted lines mark the Kroupa-like IMF slope. Grey-shaded regions show the constraints on the bimodal IMF slope from gravity-sensitive features in the SDSS spectra. Note that the lenses are in increasing order with respect to their average stellar mass. This was done to increase readability and to enable a by-eye inspection of the intersections between stellar and total mass curves. Right: similar plot for a two-segment power-law IMF. Vertical dotted lines mark a Salpeter IMF slope. See text for details.

from the lensing analysis is minimized (i.e. columns 9 and 10 in Table 3). The coloured shaded regions mark the 1σ confidence level for the constraint on the stellar mass, using the *H*- (red) and *V*- or *I*- band (blue). Note that, because of the relatively low redshift of the sample, the observed *H*-band fluxes probe the NIR rest-frame window, where the conversion from luminosity to stellar mass is less prone to the inherent degeneracies from the population parameters. Both cases use spectral fitting to constrain the stellar *M/L* (see Section 2.2). Therefore, the comparison between the optical and NIR fluxes gives an indication of the quality of the data and the goodness of fit. Note the characteristic 'U'-shaped curves for the bimodal case, with a rise in the stellar *M/L* both for low μ (dominated by remnants) and high μ (dominated by low-mass stars). The horizontal lines mark the lensing constraint, including the uncertainty (at the 90 per cent confidence level) as dashed lines. In addition, the left-hand panels show, as a grey shaded region, the 1σ constraints on the IMF slope from the analysis of the gravity-sensitive spectral indices (see Section 2.3). We emphasize that the SNR of the SDSS spectra is too low for a detailed constraint following this methodology. Nevertheless, we include this information to illustrate the compatibility with the lensing mass estimates and the stellar mass derived from spectral fitting.

It should be noted that for our study we neglect *M/L* gradients within ETGs. For ETGs only shallow gradients are expected, ranging from a minimum value of -0.1 at a characteristic mass of $\log M_s/\mathrm{M}_\odot \sim 10.3$, and increasing from there on to zero or slight positive values for most massive ETGs (Tortora et al. 2011). As we consider only the central regions, no additional trend with mass or velocity dispersion is expected.

The physical interval for the IMF slope corresponds to the region where the coloured shaded regions stay below the lensing mass. The difference between this interval and the horizontal line is the amount of additional, mostly dark matter, included within this measurement. Given that the apertures chosen are rather small (of order an effective radius), we expect the contribution from dark

matter to be small, but not negligible. We expand on this issue in Section 4.2.

Fig. 7 illustrates the range of possible IMF slopes (above $\mu > 0.8$), i.e. the interval of μ for which $M_*(\mu) < M_L$ applies. More precisely the bars start (stop) in principle when the mean stellar mass drops below (rises above) the median lens mass. The bars fill the entire range of explored slopes if the upper and lower intersections of M_* and M_L fall outside aforementioned range. However, as our analysis does not explore μ values below 0.8, the lower limit to μ remains for all lens systems (except for the lens system J1538) unconstrained by our study. Extrapolating the stellar mass curves suggests, however, a typical lower limit to μ would fall in the range of 0.5–0.8. As before red colour indicates *H*-band and blue *I* or *V* respectively. Note that the intersections of the lower (upper) limit of M_* with the upper (lower) limit to M_L give the uncertainties to respective end points of a bar. We do not include latter uncertainties in Fig. 7 for the sake of readability, but determine its average value to be ~ 0.1 for the bimodal and ~ 0.3 for the two-segment power-law IMF slope, respectively.

The plot shows that gravity-sensitive constraints on the slope of the IMF are in general consistent with the upper limits of the range of values allowed the lensing + spectral fitting analysis. Only for two lenses, J1531 and J1525, the constraints are not compatible. In J1525, we note that the 2σ lower limit from the line strength analysis is $\mu = 1.8$, well inside the allowed range of values ($\mu \lesssim 2.7$). Regarding J1531, this is one of the galaxies with the strongest NaD line strength (4.70 ± 0.14). Hence, the overly high value of the IMF slope might be driven by a Sodium overabundance, rather than a genuine bottom-heavy distribution. Indeed, excluding NaD from the line strength analysis (Section 2.3), gives $\mu = 2.4^{+2.8}_{-2.1}$, consistent with the allowed range of values for this system ($\mu < 2.3$).

We also notice that, as described in Section 4.2 below, if a significant fraction ($\gtrsim 30$ per cent) of dark matter would be present within $R_{\min}$ the combined lensing + spectral fitting analysis would give incompatible values of the IMF slope with respect to the

Table 3. Additional information of the lens sample: visual morphology, bands used in the photometric modelling, *CR rej.* indicates if CR reduction was achieved by rejection using IRAF *imcombine*, *CR LA-C* shows if additional CR reduction via LA-COSMIC (van Dokkum 2001) was required. Note that the checkmarks refer to the bands given in column 3. The *mask* and the *model* column indicate if the lensed images and arcs were either masked out or modelled using GALFIT. The colour is derived from the total luminosities in *H*-band and the blue band listed in column 3 (*Bands*), and compared to literature values in parentheses (Auger et al. 2009). $R_{\min}$, the radius of minimal uncertainty in the reconstructed lens mass profile, is given in arcsec and kpc. $\langle R/O \rangle_{\max}$ shows the quality of our photometric models, measured as the ratio between the maximum mean residual and the original flux within $R_{\min}$. M_L is the lens mass enclosed within $R_{\min}$. $M_{s,\,Kr.}$ and $M_{s,\,Salp.}$ are the stellar masses for a Kroupa and a Salpeter IMF enclosed within $R_{\min}$. The last column ($\alpha_{\mathrm{MW,\,max}}$) gives the maximum IMF normalization relative to a Kroupa IMF.

Lens ID	Morph.	Bands	CR rej.	CR LA-C	mask	model	Colour (AB)	$R_{\min}$ (arcsec)	$R_{\min}$ (kpc)	$\langle R/O \rangle_{\max}$ (per cent)	$M_L(<R_{\min})$ $\times 10^{12}$ M$_\odot$	$M_{s,\,Kr.}$ $\times 10^{12}$ M$_\odot$	M$_{s,\,Salp.}$ $\times 10^{12}$ M$_\odot$	$\alpha_{\mathrm{MW,\,max}}$
SDSSJ0037-0942	E	*H, I*	-,-	-,√	√,√	-,-	$1.02^{+0.05}_{-0.08}$ (0.71)	1.29	4.06	6.8,8.4	$0.249^{+0.013}_{-0.017}$	$0.158^{+0.026}_{-0.023}$	$0.222^{+0.031}_{-0.028}$	1.580
SDSSJ0044+0113	E	*H, V'*	√,√	√,√	-,-	√,√	$1.55^{+0.09}_{-0.09}$ (1.29)	0.60	1.26	2.9,5.6	$0.059^{+0.001}_{-0.002}$	$0.027^{+0.003}_{-0.003}$	$0.040^{+0.005}_{-0.004}$	2.158
SDSSJ0946+1006	E	*H, V'*	-,√	√,√	√,√	√,√	$1.63^{+0.08}_{-0.08}$ (1.70)	1.52	5.28	8.6,6.9	$0.318^{+0.004}_{-0.002}$	$0.114^{+0.016}_{-0.014}$	$0.166^{+0.022}_{-0.020}$	2.787
SDSSJ0955+0101	S	*H, I*	-,-	-,√	√,√	√,-	$0.88^{+0.13}_{-0.12}$ (0.89)	1.13	2.22	7.1,10.4	$0.110^{+0.004}_{-0.004}$	$0.043^{+0.006}_{-0.005}$	$0.062^{+0.009}_{-0.007}$	2.524
SDSSJ0959+0410	E	*H, V*	-,-	-,-	-,√	√,-	$1.93^{+0.08}_{-0.10}$ (1.93)	0.89	1.94	8.1,12.0	$0.070^{+0.006}_{-0.005}$	$0.030^{+0.005}_{-0.004}$	$0.045^{+0.007}_{-0.006}$	2.377
SDSSJ1100+5329	E	*H, I*	√,√	√,√	√,√	-,√	$1.22^{+0.10}_{-0.02}$ (0.89)	1.34	6.02	6.1,10.7	$0.403^{+0.016}_{-0.009}$	$0.234^{+0.055}_{-0.044}$	$0.351^{+0.075}_{-0.062}$	1.725
SDSSJ1143-0144	E	*H*	√	√	√	-	−	1.05	1.99	8.1	$0.119^{+0.017}_{-0.012}$	$0.046^{+0.005}_{-0.004}$	$0.070^{+0.008}_{-0.008}$	2.570
SDSSJ1204+0358	E	*H, V'*	√,√	√,√	-,-	√,√	$1.53^{+0.08}_{-0.08}$ (1.56)	1.24	3.39	6.2,6.6	$0.171^{+0.016}_{-0.009}$	$0.074^{+0.012}_{-0.010}$	$0.109^{+0.017}_{-0.014}$	2.314
SDSSJ1213+6708	E	*H, V'*	√,√	√,√	√,-	-,√	$1.43^{+0.06}_{-0.06}$ (1.23)	1.11	2.37	5.0,15.0	$0.117^{+0.008}_{-0.012}$	$0.055^{+0.009}_{-0.008}$	$0.084^{+0.013}_{-0.012}$	2.118
SDSSJ1402+6321	E	*H, I*	√,√	√,√	-,√	-,-	$1.06^{+0.04}_{-0.05}$ (0.75)	1.32	4.30	4.2,5.9	$0.281^{+0.003}_{-0.007}$	$0.141^{+0.029}_{-0.024}$	$0.206^{+0.041}_{-0.034}$	1.992
SDSSJ1525+3327	E	*H, V'*	√,√	√,√	-,√	√,-	$1.96^{+0.10}_{-0.13}$ (2.01)	1.19	5.79	4.2,5.0	$0.441^{+0.012}_{-0.011}$	$0.227^{+0.037}_{-0.032}$	$0.331^{+0.053}_{-0.046}$	1.938
SDSSJ1531-0105	E	*H, V'*	√,√	√,√	-,√	-,-	$1.58^{+0.06}_{-0.07}$ (1.29)	1.39	3.71	5.9,5.8	$0.195^{+0.010}_{-0.007}$	$0.132^{+0.023}_{-0.020}$	$0.185^{+0.036}_{-0.030}$	1.474
SDSSJ1538+5817	E	*H*	√	√	√	-	−	0.97	4.72	5.3	$0.087^{+0.002}_{-0.003}$	$0.058^{+0.008}_{-0.007}$	$0.085^{+0.012}_{-0.010}$	1.494
SDSSJ1630+4520	E	*H, I*	√,√	-,-	√,√	-,-	$0.96^{+0.07}_{-0.08}$ (0.97)	1.66	6.27	5.2,7.3	$0.454^{+0.024}_{-0.017}$	$0.215^{+0.035}_{-0.030}$	$0.315^{+0.047}_{-0.041}$	2.108
SDSSJ1719+2939	E/S0	*H, V'*	√,√	√,√	-,√	-,-	$1.61^{+0.08}_{-0.09}$ (1.53)	1.19	3.51	5.8, 8.9	$0.171^{+0.003}_{-0.004}$	$0.092^{+0.015}_{-0.013}$	$0.135^{+0.022}_{-0.019}$	1.853
SDSSJ2303+1422	E	*H, I*	-,-	-,-	√,√	-,√	$0.79^{+0.04}_{-0.04}$ (0.67)	1.31	3.43	5.2,5.4	$0.205^{+0.015}_{-0.012}$	$0.108^{+0.017}_{-0.015}$	$0.158^{+0.024}_{-0.021}$	1.898
SDSSJ2343-0030	E/S0	*V'*	√	-	√,-	-,√	−	1.30	3.85	5.3	$0.266^{+0.019}_{-0.018}$	$0.121^{+0.023}_{-0.020}$	$0.167^{+0.031}_{-0.026}$	2.196
SDSSJ2347-0005	E	*H, V'*	-,-	-,-	-,√	√,-	$1.99^{+0.12}_{-0.13}$ (1.97)	0.69	3.68	2.5,7.4	$0.267^{+0.037}_{-0.023}$	$0.141^{+0.020}_{-0.018}$	$0.197^{+0.039}_{-0.032}$	1.889

gravity-sensitive constraints for a significant fraction of the lenses (up to half of the total sample). Better constraints on the kinematics, and higher SNR spectra are required to address this issue in detail.

4.1 IMF normalization

In order to compare to other recent work from the literature, we present our results with respect to the IMF normalization, which is generally defined as

$$\alpha_{\mathrm{MW}} = \frac{\Upsilon_*}{\Upsilon_{*,\mathrm{MW}}} \tag{4}$$

where the numerator is the constraint on the stellar *M/L* from the analysis that varies the IMF, and the denominator is the equivalent value when the IMF is fixed to the fiducial IMF adopted for the Milky Way. Depending on the study, this reference is either a Salpeter or a Kroupa IMF. Hereafter we will adopt the Kroupa normalization as the IMF reference for the Milky Way.

Fig. 8 shows our constraints on the IMF normalization with respect to the velocity dispersion derived from the SDSS spectra (using our STARLIGHT runs). Note the low-μ branch (i.e. top-heavy IMFs) is usually unconstrained with respect to lensing: most of the coloured regions in the left-hand panels of Fig. 6 fall below the lensing mass at low values of μ. Although we cannot constrain this branch of the IMF with lensing data, the gravity-sensitive index analysis (e.g. La Barbera et al. 2013) or the number of X-ray binary sources (e.g. Weidner et al. 2013) gives significant evidence against highly top-heavy IMFs in massive ETGs. The upper limit of α_{MW}

is defined for the value of μ where the stellar mass equals the total, lensing, mass. The lower limit of α_{MW} is determined by the minimal value of the lower limit to the stellar mass curve in Fig. 6. Note that the intersection between the red *x*- and *y*-error bars in Fig. 8 refers to the mean value of the range of possible stellar masses, i.e. $[M_L + \min(M_s(\mu))]/2$. For reference, we include the results from Treu et al. (2010) (grey dots) and Posacki et al. (2015) (solid line), and the four lenses from Smith et al. (2015) (blue dots), that feature an intriguingly low stellar *M/L*, at odds with results, based on gravity-sensitive features, for galaxies with similar sigma. Our constraints are consistent with the results of Posacki et al. (2015). Note that with respect to Posacki et al. (2015), we follow a different approach for the modelling of the lens (see Section 2.4). Moreover, we constrain the stellar *M/L* consistently fitting population synthesis models over a wide range of choices of the IMF (see Section 2.2). The orange circles represent the α_{MW} values of Treu et al. (2010) at the velocity dispersion values derived from STARLIGHT. Note that our methodology is different from this work, as we perform spectral fitting using a variable IMF to constrain the stellar IMF. In Fig. 9 we show a similar plot, replacing the velocity dispersions measured on the spectra by the ones inferred from the lensing data via the virial theorem (see Leier 2009, for an example of the use of these indirect velocity dispersions). Note that the orange circles highlight the common subset of the SLACS lenses from Treu et al. (2010) and this study. The result is very similar, although two of the lenses (J2347 and J1525) could be in a similar region as the lenses of Smith et al. (2015) if we assume a very large amount of dark matter ($\gtrsim 30$ per cent). This scenario is rather unlikely given that the
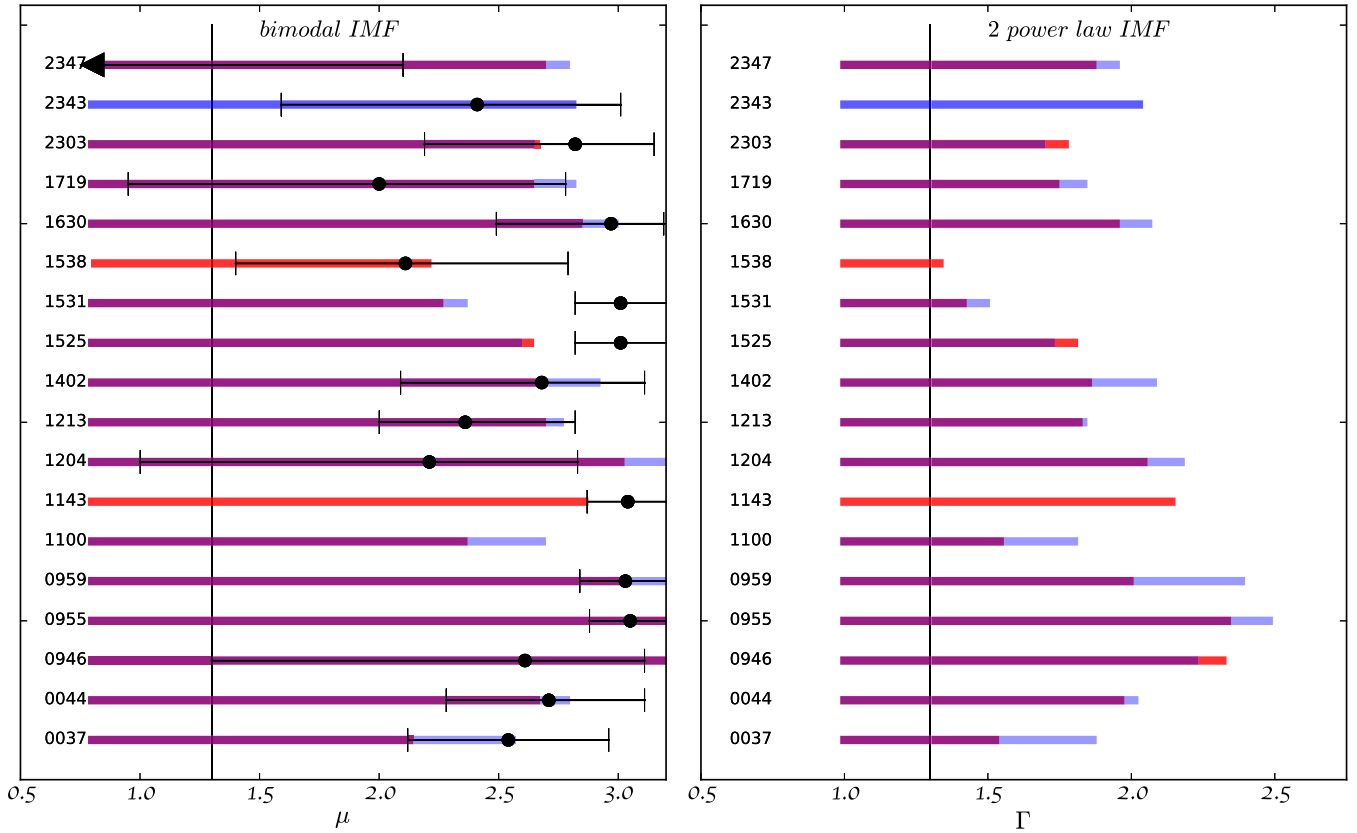
Figure 7. Left: the horizontal bars represent the range of IMF slopes that give a physically acceptable solution (i.e. where the mean M_s lies below the median M_{tot}, measured within $R < R_{min}$). Note that the μ-range below 0.8 is not explored in this study. Red (blue) indicates constraints from *H*-band (*V/I*-band) photometry. A magenta bar shows IMF slopes for which both *H*-band and the corresponding blue band constraints are in agreement. The black dot and error bars represent the best fit and 1σ confidence level of the constraint from the analysis of gravity-sensitive line strengths (see Section 2.3). Right: equivalent results for the parametrization using a two-segment power-law function.
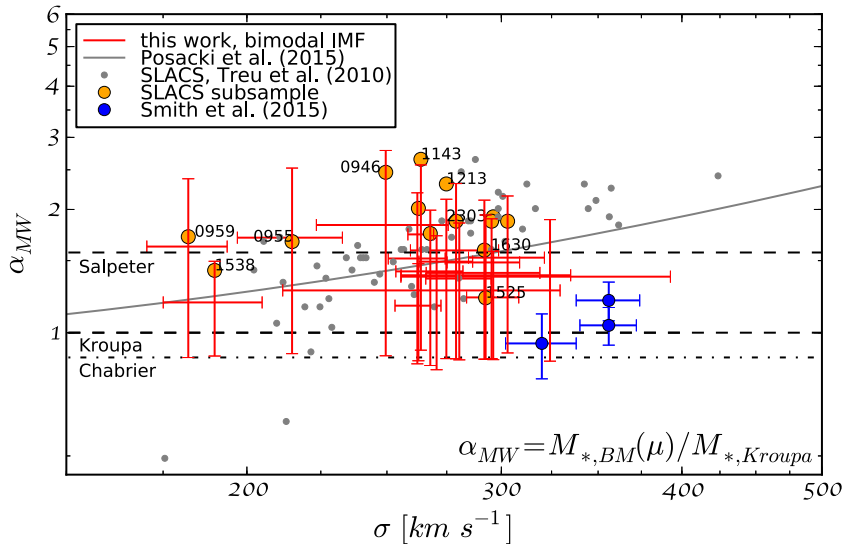
Figure 8. The IMF normalization factor α_{MW} is plotted versus velocity dispersion, adjusted to $\sigma(R_e/8)$. α_{MW} is defined with respect to a Kroupa (2001) IMF, as in Smith et al. (2015). The orange circles represent the subsample of the SLACS lenses of Treu et al. (2010) used in this study. The four SLACS lenses, J1100, J1719, J2343 and J2347, were not included in the work by Treu et al. (2010) and have hence no orange circle. Note that the highest possible normalization factor corresponds to a scenario where no dark matter is measured within R_{min}. The lowest possible normalization factor corresponds to the lower limit of the minimum of the stellar mass curves in Fig. 6 (left-hand panel). It is thus a consequence of the IMF choice and independent of the data.
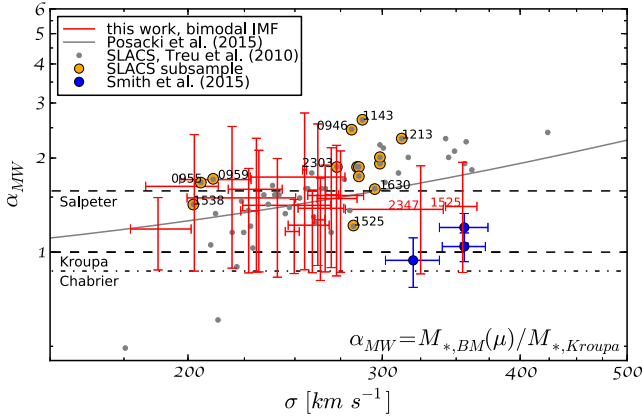
Figure 9. As in Fig. 8 but with velocity dispersions inferred from lensing by assuming the virial theorem, corrected to an aperture of $R_e/8$.

apertures are comparable to the effective radius. In the next section, we determine with a simple model the expected contribution of dark matter in these measurements.

4.2 Dark matter contribution

The constraints on the stellar *M/L* presented in this work are the most robust ones regarding spectral fitting: we fit the SDSS spectra using a large volume of parameter space that includes the latest population synthesis models of Bruzual & Charlot (2003) for a range of ages, metallicities, and IMF slope. However, the comparison with lensing masses is complicated by the presence of additional components. Our sample is made up of ETGs, where gas and dust contribute a negligible fraction to the mass budget within the apertures explored (of order an effective radius). However, we need to provide estimates for the contribution of dark matter. Note that in order to keep the results as robust as possible, we do not deproject our data. Nevertheless, in this section we calculate the expected fraction of dark matter for the typical cases commonly adopted in the literature. We consider a spherically symmetric dark matter halo with the density slope of Navarro, Frenk & White (1997, hereafter NFW).

For the sample of lenses used in this study, we determine a mean $R_{\min}/R_e$ value of 0.7 in contrast to 2.3, which is an average value for CASTLeS lenses[5] studied in Leier et al. (2011). This indicates that the region of interest – where the uncertainties in the lensing mass are smallest – is probably dominated by baryonic matter in the form of stars.

As the Einstein radii of SLACS lenses are typically small and thus not sensitive to the turn-over at r_s, NFW fits to the enclosed dark matter profile – defined as the difference of total enclosed mass and stellar mass – are far too unconstrained to produce reliable numbers. Assuming a fixed scale radius of $r_s = 30$ kpc to infer $M_s/M_{DM}(<R_{\min})$, as shown in Treu et al. (2010), introduces a bias as it leads to concentrations R_{vir}/r_s increasing with M_{vir}, a consequence of $R_{vir} \propto M_{vir}^{1/3}$. This trend is firmly excluded by simulations and observational studies. In fact in a previous study comprising 18 lens galaxies from the CASTLeS sample (Leier et al. 2012), we were able to determine a lower median scale radius of the NFW profile of $11.1^{+26.0}_{-7.6}$ kpc (90 per cent confidence level). For reference, the Hernquist scale radius, adopted for the stellar component, gave a

<hr>

[5] Note that, in general, the CASTLeS sample is at higher redshift than the SLACS data set.
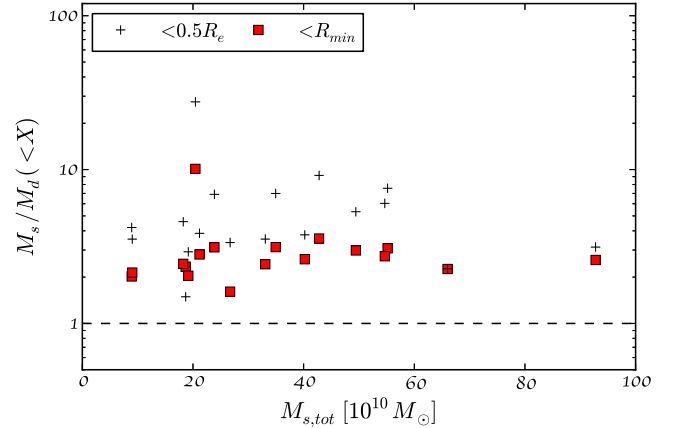
Figure 10. The fraction of the enclosed stellar over dark matter (in projection) is shown with respect to total stellar mass. Note that the stellar-to-dark matter fractions are derived from the halo-to-stellar mass relation of Moster et al. (2010), including assumptions about the profiles of each component, as explained in the text. Squares denote a radius of enclosure of $R_{\min}$ (given in Table 3), i.e. the radius of minimal uncertainty from the ensemble of lens models, which is roughly equal to the Einstein radius. Crosses refer to a radius of enclosure of half the effective radius. The dashed line indicates equal amounts of stellar and dark matter.

median of $r_{Hern} = 1.85^{+0.73}_{-0.78}$ kpc. In view of the considerable scatter in r_s, we choose to model the median dark matter profile with NFW fits. As the fits are otherwise relatively unconstrained, we add additional information by means of the stellar-to-halo mass relation derived by Moster et al. (2010). Using the results from abundance matching, we compute $M_{DM}(<R_{vir})$ inside the virial radius plus uncertainties based on the total stellar mass of the lens galaxy.

We want to emphasize here that for $M_s > 10^{13}\,M_\odot$ all stellar-to-halo mass relations follow a shallow power law which comes with a large uncertainty with respect to the halo mass. The uncertainties of M_s increase the uncertainties of M_{halo} found by abundance matching even further. By doing so we get uncertainties which are in agreement with stellar-to-halo mass relations based on a variety of different IMF models including systematic variations with circular velocity investigated by McGee, Goto & Balogh (2014).

The same method was tested in our previous study by means of CASTLeS lenses whose mass profile could be probed to larger radii (Leier et al. 2012). We found that for most of our lenses, that reside in less dense environments, fits to the enclosed mass $M_{DM}(<2R_{\min})$ are in good agreement with $M_{halo}(<R_{vir})$ from the stellar-to-halo mass relation. The stellar mass profile is fit with a Hernquist profile. The best-fitting results of the stellar to dark matter mass ratio are shown in Fig. 10.

As the Einstein radius of SLACS lenses are small and mostly insensitive to the turn-over at r_s, the above assumption of a fixed 30 kpc is justified. However, the scale radius to 30 kpc is problematic as it leads to a monotonic increase in concentration with M_{vir}. This is a result of r_{vir} and thus r_{vir}/r_s increasing with virial mass. This trend is firmly excluded by simulations and observational studies. In a follow-up paper, we will investigate in detail the relation of baryonic and dark-matter scale parameters, concentrations and their dependency on the collapse redshift in top-hat collapse models.

By assuming additional information on the halo mass within R_{vir}, using the best-fitting NFW profile to calculate the enclosed masses, we obtain a median value $M_s/M_{DM}(<R_{\min}) = 2.59^{+0.55}_{-0.56}$ (68 per cent confidence level). The same ratio enclosed within $0.5\,R_e$ yields $3.85^{+3.64}_{-1.51}$. Therefore, we conclude that there is roughly between 2
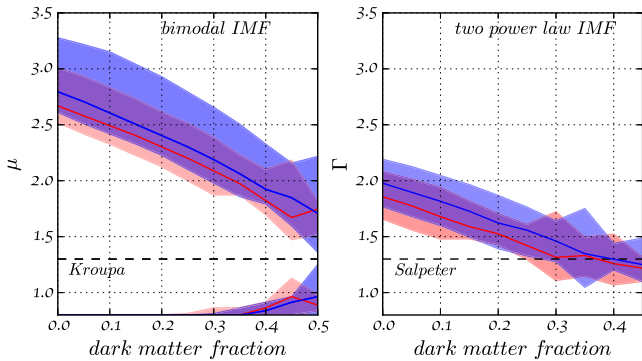
Figure 11. IMF parameters versus dark matter fraction (f_{DM}). an increase in the DM fraction causes the α-interval to shrink and the IMF parameter interval, defined by the intersection of $(1 - f_{DM}) \times M_{tot}$ and M_* to shift. Median (solid line) and 68 per cent confidence intervals (shaded region) are shown for the whole set of lenses. Red (blue) colour denotes *H*-band (I, *V*-band) data. The left-hand panel shows the results for a bimodal IMF parametrization, hence the two separate μ-intervals. The right-hand panel shows the two-segment power-law parametrization, which constrains Γ only from one side.

and 4 times more stellar mass than dark matter within the central region of our lensing galaxies. However, in view of the considerable uncertainties attached to the fit parameters, we are not accepting the inferred stellar-to-dark matter fractions at its face-value but rather as a rough indicator of what we can expect from more detailed follow-up studies. Note that other choices of IMF and systematic variations of such could lead to a more extreme flattening of the stellar-to-halo mass relation leading to even larger dark matter fraction, strengthening our argument against very bottom heavy IMFs.

As we find evidence for a non-negligible dark matter fraction, we proceed by evaluating our findings over the range of IMF slopes presented in Fig. 6. A non-zero dark matter fraction causes the range of IMF normalization values (α_{MW}) to shrink. Moreover, the interval of allowed IMF slopes, defined by the intersection of $(1 - f_{DM}) \times M_{tot}$ and M_* changes as well. This is shown in Fig. 11. For a certain dark matter fraction, we compute the median and the 68 per cent confidence intervals of this IMF allowed range. *H*-band and blue band constraints present equal trends and agree within uncertainties. For the bimodal IMF (Fig. 11, left-hand panel) the general trend disfavours MW-like IMFs even for dark matter fractions as high as 50 per cent. However, due to the typical u-shape of the stellar *M/L* as a function of the bimodal slope (μ) (left plot of Fig. 6), a top-heavy IMF (low value of μ) can produce stellar masses in agreement with our lensing constraints. For the two-segment power-law parametrization (Fig. 11, right-hand panel) we find that agreement between a Salpeter IMF and the range of slopes (Γ) can be achieved for much smaller dark matter fractions ($\sim$25 per cent).

5 SUMMARY AND CONCLUSIONS

This paper focuses on constraints to the stellar *M/L* of a sample of 18 strong gravitational lenses from the SLACS data base, in context with the recent findings of a systematic variation of the IMF in ETGs. For each lens, the SDSS spectrum is fitted to the latest set of population synthesis models from Bruzual & Charlot (2003), to infer a probability distribution function of the stellar *M/L* over a range of population parameters. In addition to a range of SFHs and chemical composition, the population models include a wide range of IMF choices, from top-heavy to bottom-heavy models, adopting

both a bimodal IMF and a two-segment power-law mass function. The constraints on the stellar *M/L* are combined with optical and NIR photometric models of the SB distribution to determine stellar masses. Independently, we derive the projected lensing mass, and compare both within an aperture for which the lensing uncertainties are minimized. The geometry of the lenses from the SLACS data base is such that the Einstein radius probes the central regions of massive galaxies, the ideal case to test the observed variations of the IMF (see, e.g. van Dokkum & Conroy 2010; Ferreras et al. 2013; La Barbera et al. 2013), where the contribution from dark matter to the lensing signal is smallest. Regardless of any dark matter model, we are able to robustly reject the heaviest choices of the IMF, although in most cases there is no substantial tension between these constraints and those from gravity-sensitive spectral features. Only for J1525+3327 and J1531-0105, a similar disagreement is found, as in Smith et al. (2015), with stellar *M/L* consistent with the standard, Milky Way IMF. Note, however, that the redshifts of the Smith et al. (2015) lenses are significantly lower than in SLACS, hence corresponding to smaller R_{Ein}/R_{eff}, and therefore to smaller contributions from dark matter.

For the bimodal parametrization we find that, on average, the upper limit lies around $\mu \lesssim 2.6$. This limit is rather robust, as it corresponds to a scenario where no dark matter is present within the aperture. Higher values of μ, aside from an unknown systematic, are therefore unphysical. The two-segment power-law parametrization of the IMF is much more constraining, ruling in general models where $\Gamma > 1.7$. However, note the Salpeter equivalent ($\Gamma = 1.3$) is compatible with all lenses (if a non-zero dark matter fraction is assumed), including J1538+5817. This lens gives the strongest constraint against a bottom-heavy IMF. The bimodal functional form is preferred over other choices for which the contribution from low-mass stars increases sharply with slope, such as a single power law (La Barbera et al. 2016). Our two-segment power-law prescription is similar to a single power law in the sense that a varying Γ introduces a sharp increase of the contribution from low-mass stars. Therefore, from these two options, we would favour the bimodal functional form.

If we include in the lensing budget a non-zero dark matter component based on the reconstructed median profile and a halo mass from abundance matching results (Moster et al. 2010), we estimate from sample statistics a contribution within the measurement aperture (R_{min}) around 28 per cent, although the dark matter contribution can be as low as 10 per cent. This will further constrain the results towards a lighter IMF. Nevertheless, our results allow for values around $\mu \lesssim 2.0$ ($\Gamma \lesssim 1.5$) even if the dark matter amounts to 30 per cent of the lensing mass. This upper bound is consistent with the constraints derived from gravity-sensitive line strengths. For instance, taking the IMF slope versus velocity dispersion relationship from La Barbera et al. (2013) for 2SSP models allowing for individual abundance variations ([Na/Fe], [Ca/Fe] and [Ti/Fe]) give a constraint of the bimodal IMF of $\mu = 2.2 \pm 0.2$ (1σ).

In addition, we note that even though the sample has a relatively narrow range in velocity dispersion (mostly around $250 \, \mathrm{km \, s^{-1}}$), there is a wide range of IMF slopes allowed by our analysis that may be responsible for the low stellar *M/L* found by Smith et al. (2015) in a reduced set of lenses.
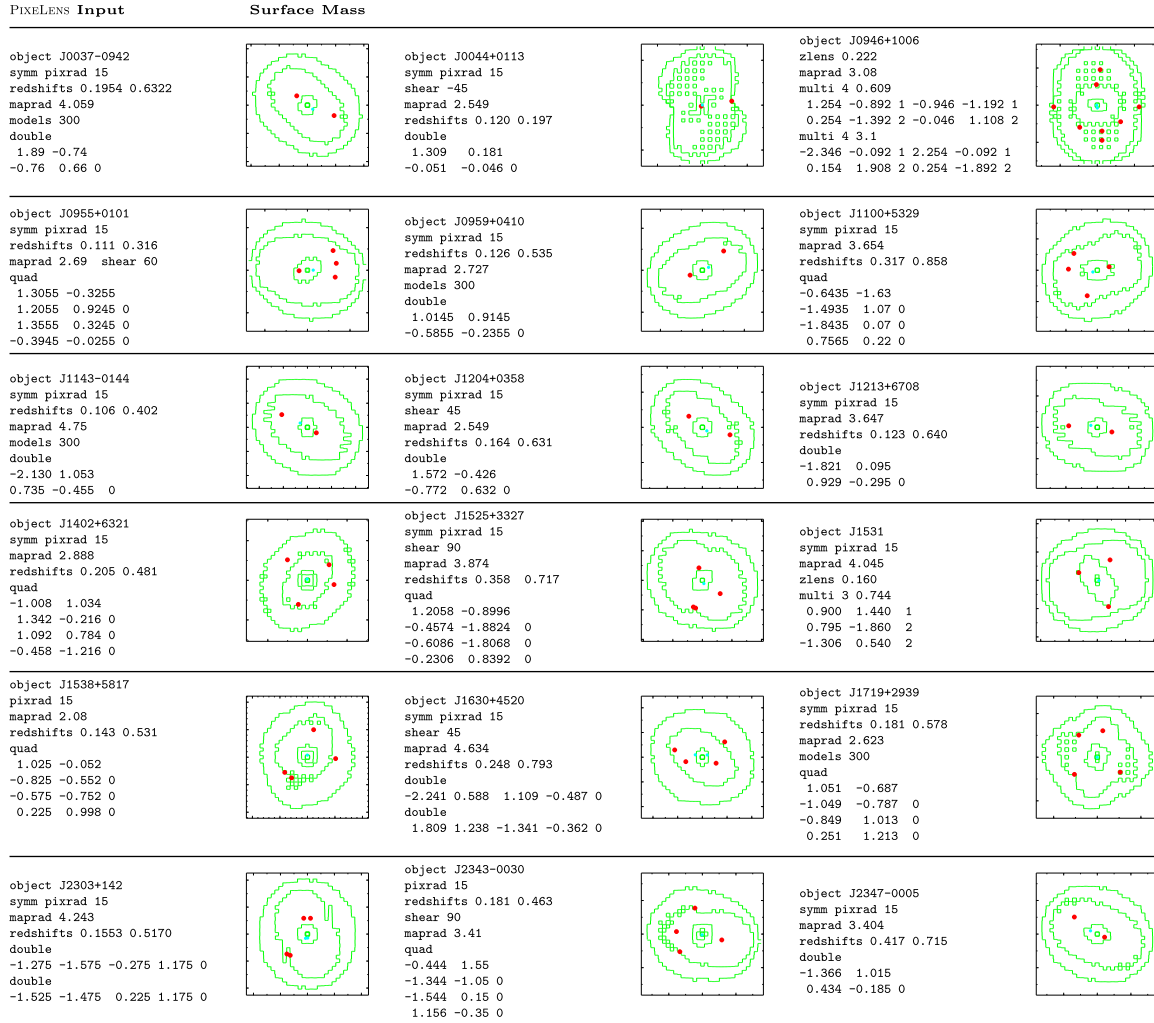
REFERENCES

Auger M. W., 2008, MNRAS, 383, L40

Auger M. W., Treu T., Bolton A. S., Gavazzi R., Koopmans L. V. E., Marshall P. J., Bundy K., Moustakas L. A., 2009, ApJ, 705, 1099

Auger M. W., Treu T., Gavazzi R., Bolton A. S., Koopmans L. V. E., Marshall P. J., 2010, ApJ, 721, L163

Benítez N., 2000, ApJ, 536, 571

Bolton A. S., Burles S., Koopmans L. V. E., Treu T., Moustakas L. A., 2006, ApJ, 638, 703

Bressan A., Marigo P., Girardi L., Salasnich B., Dal Cero C., Rubele S., Nanni A., 2012, MNRAS, 427, 127

Bruzual G., Charlot S., 2003, MNRAS, 344, 1000

Cappellari M. et al., 2012, Nature, 484, 485

Cappellari M. et al., 2013, MNRAS, 432, 1862

Cardelli J. A., Clayton G. C., Mathis J. S., 1989, ApJ, 345, 245

Cenarro A. J., Gorgas J., Vazdekis A., Cardiel N., Peletier R. F., 2003, MNRAS, 339, L12

Chabrier G., 2003, PASP, 115, 763

Chabrier G., Hennebelle P., Charlot S., 2014, ApJ, 796, 75

Cid Fernandes R., Mateus A., Sodré L., Stasinska G., Gomes J. M., 2005, MNRAS, 358, 363

Coles J. P., 2008, ApJ, 679, 17

Coles J. P., Read J. I., Saha P., 2014, MNRAS, 445, 2181

Conroy C., van Dokkum P., 2012a, ApJ, 747, 69

Conroy C., Graves G. J., van Dokkum P. G., 2014, ApJ, 780, 33

de la Rosa I. G., La Barbera F., Ferreras I., de Carvalho R. R., 2011, MNRAS, 418, L74

Dominik M., 1999, A&A, 349, 108

Drinkwater M. J. et al., 2010, MNRAS, 401, 1429

Dutton A. A., Mendel J. T., Simard L., 2012, MNRAS, 422, L33

Falcón-Barroso J. Sánchez-Blázquez P., Vazdekis A., Ricciardelli E., Cardiel N., Cenarro A. J., Gorgas J., Peletier R. F., 2011, A&A, 532, 95

Ferré-Mateu A., Vazdekis A., de la Rosa I. G., 2013, MNRAS, 431, 440

Ferreras I., Saha P., Burles S., 2008, MNRAS, 383, 857

Ferreras I., Saha P., Leier D., Courbin F., Falco E. E., 2010, MNRAS, 409, L30

Ferreras I. et al., 2012, AJ, 144, 47

Ferreras I., La Barbera F., de la Rosa I. G., Vazdekis A., de Carvalho R. R., Falcón-Barroso J., Ricciardelli E., 2013, MNRAS, 429, L15

Gal R. R., de Carvalho R. R., Lopes P. A. A., Djorgovski S. G., Brunner R. J., Mahabal A., Odewahn S. C., 2003, AJ, 125, 2064

Gavazzi R., Treu T., Koopmans L. V. E., Bolton A. S., Moustakas L. A., Burles S., Marshall P. J., 2008, ApJ, 677, 1046

Geach J. E., Murphy D. N. A., Bower R. G., 2011, MNRAS, 413, 3059

Grillo C., Eichner T., Seitz S., Bender R., Lombardi M., Gobat R., Bauer A., 2010, ApJ, 710, 372

Häussler B. et al., 2007, ApJS, 172, 615

Hopkins P. F., 2013, MNRAS, 433, 170

Krist J., 1995, ASP Conf., 77, 349

Kroupa P., 2001, MNRAS, 322, 231

La Barbera F., Ferreras I., Vazdekis A., de la Rosa I. G., de Carvalho R. R., Trevisan M., Falcón-Barroso J., Ricciardelli E., 2013, MNRAS, 433, 3017

La Barbera F., Ferreras I., Vazdekis A., 2015, MNRAS, 449, L137

La Barbera F., Vazdekis A., Ferreras I., Pasquali A., Cappellari M., Martín-Navarro I., Schönebeck F., Falcón-Barroso J., 2016, MNRAS, 457, 1468

Leier D., 2009, MNRAS, 400, 875

Leier D., Ferreras I., Saha P., Falco E. E., 2011, ApJ, 740, 97

Leier D., Ferreras I., Saha P., 2012, MNRAS, 424, 104

McConnachie A. W., Patton D. R., Ellison S. L., Simard L., 2009, MNRAS, 395, 255

McGee S. L., Goto R., Balogh M. L., 2014, MNRAS, 438, 3188

Marigo P., Bressan A., Nanni A., Girardi L., Pumo M. L., 2013, MNRAS, 434, 488

Miller G. E., Scalo J. M., 1979, ApJS, 41, 513

Moster B. P., Somerville R. S., Maulbetsch C., van den Bosch F. C., Macciò A. V., Naab T., Oser L., 2010, ApJ, 710, 903

Navarro J. F., Frenk C. S., White S. D. M., 1997, ApJ, 490, 493 (NFW)

Newton E. R., Marshall P. J., Treu T., Auger M. W., Gavazzi R., Bolton A. S., Koopmans L. V. E., Moustakas L. A., 2011, ApJ, 734, 104

Pacifici C. et al., 2015, MNRAS, 447, 786

Padoan P., Nordlund Å., 2002, ApJ, 576, 870

Peng C. Y., Ho L. C., Impey C. D., Rix H.-W., 2010, AJ, 139, 2097

Posacki S., Cappellari M., Treu T., Pellegrini S., Ciotti L., 2015, MNRAS, 446, 493

Rines K., Geller M. J., Kurtz M. J., Diaferio A., 2003, AJ, 126, 2152

Saha P., Williams L. L. R., 2004, AJ, 127, 2604

Salpeter E. E., 1955, ApJ, 121, 161

Sánchez-Blázquez P. et al., 2006, MNRAS, 371, 703

Schlafly E. F., Finkbeiner D. P., 2011, ApJ, 737, 103

Seigar M. S., Graham A. W., Jerjen H., 2007, MNRAS, 378, 1575

Simha V., Weinberg D. H., Conroy C., Dave R., Fardal M., Katz N., Oppenheimer B. D., 2014, preprint (arXiv:1404.0402)

Slezak E., Durret F., Guibert J., Lobo C., 1998, A&AS, 128, 67

Smith R. J., 2014, MNRAS, 443, L69

Smith R. J., Lucey J. R., 2013, MNRAS, 434, 1964

Smith R. J., Lucey J. R., Conroy C., 2015, MNRAS, 449, 3441

Sonnenfeld A., Treu T., Gavazzi R., Marshall P. J., Auger M. W., Suyu S. H., Koopmans L. V. E., Bolton A. S., 2012, ApJ, 752, 163

Spiniello C., Trager S., Koopmans L. V. E., Conroy C., 2014, MNRAS, 438, 1483

Spinrad H., 1962, PhD thesis, UC Berkeley

Tessore N., Bellagamba F., Metcalf R. B., 2015, preprint (arXiv:1505.07674)

Tody D., 1993, in Hanisch R. J., Brissenden R. J. V., Barnes J., eds, ASP Conf. Ser. Vol. 52, Astronomical Data Analysis Software and Systems II. Astron. Soc. Pac., San Francisco, p. 173

Tortora C., Napolitano N. R., Romanowsky A. J., Jetzer P., Cardone V. F., Capaccioli M., 2011, MNRAS, 418, 1557

Treu T., Auger M. W., Koopmans L. V. E., Gavazzi R., Marshall P. J., Bolton A. S., 2010, ApJ, 709, 1195

van Dokkum P. G., 2001, PASP, 113, 1420

van Dokkum P. G., Conroy C., 2010, Nature, 468, 940

Vazdekis A., Casuso E., Peletier R. F., Beckman J. E., 1996, ApJS, 106, 307

Vazdekis A., Cenarro A. J., Gorgas J., Cardiel N., Peletier R. F., 2003, MNRAS, 340, 1317

Vazdekis A., Ricciardelli E., Cenarro A. J., Rivero-González J. G., Díaz-García L. A., Falcón-Barroso J., 2012, MNRAS, 424, 157

Weidner C., Ferreras I., Vazdekis A., La Barbera F., 2013, MNRAS, 435, 2274

PixeLens Input   Surface Mass

```
object J0037-0942
symm pixrad 15
redshifts 0.1954 0.6322
maprad 4.059
models 300
double
 1.89 -0.74
-0.76  0.66 0
```

```
object J0044+0113
symm pixrad 15
shear -45
maprad 2.549
redshifts 0.120 0.197
double
 1.309   0.181
-0.051  -0.046 0
```

```
object J0946+1006
zlens 0.222
maprad 3.08
multi 4 0.609
 1.254 -0.892 1 -0.946 -1.192 1
 0.254 -1.392 2 -0.046 1.108 2
multi 4 3.1
-2.346 -0.092 1 2.254 -0.092 1
 0.154  1.908 2 0.254 -1.892 2
```

```
object J0955+0101
symm pixrad 15
redshifts 0.111 0.316
maprad 2.69  shear 60
quad
 1.3055 -0.3255
 1.2055  0.9245 0
 1.3555  0.3245 0
-0.3945 -0.0255 0
```

```
object J0959+0410
symm pixrad 15
redshifts 0.126 0.535
maprad 2.727
models 300
double
 1.0145  0.9145
-0.5855 -0.2355 0
```

```
object J1100+5329
symm pixrad 15
maprad 3.654
redshifts 0.317 0.858
quad
-0.6435 -1.63
-1.4935  1.07 0
-1.8435  0.07 0
 0.7565  0.22 0
```

```
object J1143-0144
symm pixrad 15
redshifts 0.106 0.402
maprad 4.75
models 300
double
-2.130 1.053
0.735 -0.455  0
```

```
object J1204+0358
symm pixrad 15
shear 45
maprad 2.549
redshifts 0.164 0.631
double
 1.572 -0.426
-0.772  0.632 0
```

```
object J1213+6708
symm pixrad 15
maprad 3.647
redshifts 0.123 0.640
double
-1.821  0.095
 0.929 -0.295 0
```

```
object J1402+6321
symm pixrad 15
maprad 2.888
redshifts 0.205 0.481
quad
-1.008  1.034
 1.342 -0.216 0
 1.092  0.784 0
-0.458 -1.216 0
```

```
object J1525+3327
symm pixrad 15
shear 90
maprad 3.874
redshifts 0.358  0.717
quad
 1.2058 -0.8996
-0.4574 -1.8824  0
-0.6086 -1.8068  0
-0.2306  0.8392  0
```

```
object J1531
symm pixrad 15
maprad 4.045
zlens 0.160
multi 3 0.744
 0.900  1.440  1
 0.795 -1.860  2
-1.306  0.540  2
```

```
object J1538+5817
pixrad 15
maprad 2.08
redshifts 0.143 0.531
quad
 1.025 -0.052
-0.825 -0.552 0
-0.575 -0.752 0
 0.225  0.998 0
```

```
object J1630+4520
symm pixrad 15
shear 45
maprad 4.634
redshifts 0.248 0.793
double
-2.241 0.588  1.109 -0.487 0
double
 1.809 1.238 -1.341 -0.362 0
```

```
object J1719+2939
symm pixrad 15
redshifts 0.181 0.578
maprad 2.623
models 300
quad
 1.051  -0.687
-1.049  -0.787  0
-0.849   1.013  0
 0.251   1.213  0
```

```
object J2303+142
symm pixrad 15
maprad 4.243
redshifts 0.1553 0.5170
double
-1.275 -1.575 -0.275 1.175 0
double
-1.525 -1.475  0.225 1.175 0
```

```
object J2343-0030
pixrad 15
redshifts 0.181 0.463
shear 90
maprad 3.41
quad
-0.444  1.55
-1.344 -1.05 0
-1.544  0.15 0
 1.156 -0.35 0
```

```
object J2347-0005
symm pixrad 15
maprad 3.404
redshifts 0.417 0.715
double
-1.366  1.015
 0.434 -0.185 0
```

Figure A1. PixeLens input data and projected mass distributions for the lens sample. For all lenses an ensemble of 300 mass models is computed in a radial aperture of roughly twice the Einstein radius, corresponding to 15 pixels. Further lens properties are given in Table 3.

APPENDIX A: LENS MODELS

In Fig. A1 we present the PixeLens inputs and free-form surface mass models used in this study. For all lenses an ensemble of 300 models is computed. The coordinates are taken from the brightest pixels within a lensed image.

The 'shear' term in the PixeLens input refers to external shear from other galaxies. In 6 out of the 18 lens systems, the environment showed evidence for significant external shear (see Section 3). In these cases, we allowed external shear, aligned within $45°$ of a visually set preliminary orientation. The symmetric shear-matrix elements g_{11}, g_{22} and g_{12} are given in Table A1. In addition, there is always some internal shear due to the mass distribution of the main lensing galaxy. The internal and external shears are partly degenerate (cf. Dominik 1999), and hence the external shear is partly degenerate with R_{min} as well, but the resulting variation is included within the quoted uncertainties.

Table A1. Median shear matrix elements and 90 per cent confidence limits. Note that if g_{11} and g_{22} show zero uncertainty, while g_{12} is uncertain the interpretation is that the shear uncertainty is closely aligned with the 'x' shear direction.

ID	g_{11}	g_{22}	g_{12}
J0044	$0.07^{+0.00}_{-0.00}$	$0.07^{+0.00}_{-0.07}$	$0.10^{+0.00}_{-0.07}$
J0955	$0.00^{+0.01}_{-0.01}$	$0.00^{+0.01}_{-0.03}$	$0.00^{+0.03}_{-0.00}$
J1204	$0.00^{+0.00}_{-0.03}$	$0.00^{+0.00}_{-0.03}$	$0.00^{+0.04}_{-0.00}$
J1525	$0.00^{+0.01}_{-0.02}$	$0.00^{+0.00}_{-0.04}$	$0.00^{+0.04}_{-0.00}$
J1630	$-0.01^{+0.02}_{-0.04}$	$-0.01^{+0.01}_{-0.05}$	$0.02^{+0.07}_{-0.02}$
J2343	$0.00^{+0.03}_{-0.00}$	$0.00^{+0.03}_{-0.01}$	$0.00^{+0.04}_{-0.00}$

This paper has been typeset from a TeX/LaTeX file prepared by the author.